

Recent developments of the Material Point Method for the simulation of landslides

This content has been downloaded from IOPscience. Please scroll down to see the full text.

2015 IOP Conf. Ser.: Earth Environ. Sci. 26 012003

(<http://iopscience.iop.org/1755-1315/26/1/012003>)

View [the table of contents for this issue](#), or go to the [journal homepage](#) for more

Download details:

IP Address: 147.83.51.251

This content was downloaded on 18/01/2016 at 22:50

Please note that [terms and conditions apply](#).

Recent developments of the Material Point Method for the simulation of landslides

E E Alonso¹, A Yerro and N M Pinyol

Department of Geotechnical Engineering & Geosciences, Universitat Politècnica de Catalunya-BarcelonaTech, Barcelona, Spain

E-mail: eduardo.alonso@upc.edu

Abstract. The paper describes first the theoretical framework of a “single layer” three phase material. The formulation is general and particular cases are dry and fully saturated soils. The formulation and discretization of the motion and balance equations is presented. Two constitutive equations are used in the applications described: A brittle model for saturated soils and a Mohr-Coulomb elastoplastic soil formulated in terms of net stress and suction. Three aspects of the behaviour of landslides are discussed: first time failures in over-consolidated clays; internal shearing in deep seated landslides and rain induced failures in unsaturated slopes. The discussion is supported by three real cases which are described and analyzed in detail.

1. Introduction

Material Point Methods (MPM) are rapidly evolving in the geotechnical field especially in slope stability problems. This is because of their capability to analyze the whole instability problem in a unified calculation including the transition from the pre-failure stage, characterized by the development of small strains, to the accelerated post-rupture phase in which large deformations of the sliding mass are involved.

Based on particle methods, MPM [1] discretizes the continuum by means of material points. Each such a point moves attached to the portion of media that represents, giving a Lagrangian description of the motion, and carrying all the information (strain, stresses, pressure, mass...). On the other hand, main governing equations are posed and solved at the nodes of a background mesh in a very similar way as it is done in finite element methods (FEM). However, the integration points are the material points themselves instead of the typical Gaussian quadrature. The mesh covers the whole computational domain and usually it is maintained fixed throughout the calculation. In this manner, most of the expertise learned from FEM can be applied to the MPM with the additional improvement that large deformations can be simulated without limitations of mesh tangling. Linear shape functions

¹ Department of Geotechnical Engineering and Geosciences.
Universitat Politècnica de Catalunya-BarcelonaTech, Campus Nord
C/ Jordi Girona 1-3, Edificio D-2. 08034 Barcelona
Phone: +34 93 401 6866; +34 93 401 7256
Fax: +34 93 401 7251
e-mail: eduardo.alonso@upc.edu



are typically used in order to transfer information between both discretization levels (nodes and material points). Moreover, another advantage of the MPM discretization is that it is well suited for history-dependent constitutive models. This is a very important capability, especially in landslide analysis where material properties can change during the instability process (degradation due to extensive shearing).

Three relevant aspects for the interpretation of Landslides are described in the paper. The first topic concerns the development of progressive failure and subsequent post-failure behavior in brittle materials. This is the case in first time failures in overconsolidated clays. The failure results in an accelerated motion. The case analyzed: The Selborne failure experiment illustrates this class of instabilities.

The second aspect analyzed focuses on the kinematics of deep seated landslides and, in particular, in the role played by internal shearing of rock masses. Compound landslides are possible if internal rock strength is exhausted along surfaces or shearing bands which make the motion kinematically admissible. The well-known case of Vaiont is examined from this perspective.

The final case deals with the stability of unsaturated slopes under rainfall. A case inspired in the surface ruptures experienced by some embankment slopes will be presented and discussed.

2. Theoretical framework

2.1. Basis of MPM

MPM was initially developed for solid mechanics [2]. However, the slope stability is closely related to changes in water table conditions due to climate effects, such as heavy rainfall or wetting-drying cycles. Therefore, in landslide prediction analysis coupled hydro-mechanical formulations are particularly useful because they are capable of modelling interaction between solid skeleton and fluid within the porous media or even with free water. During the last decade, the classic MPM formulation has been extended to solve multiphase problems and basically two approaches can be distinguished: the “single-layer” and the “multi-layer” one.

The “single-layer” strategy is the most extended formulation. It is based on representing the porous medium as a unique continuum by means a set of material points. Thus each point moves according to the solid skeleton motion, but also carries information of pore fluids -water and air in unsaturated media- as internal variables. This approach is appropriate to simulate seepage problems but it is not capable to model free liquid water. It has been adopted by several authors to solve problems in saturated conditions (two-phases) [3][4][5][6], and it has also been extended to unsaturated problems in Yerro et al. [6] (three-phases). The “multi-layer” approach represents each constituent -grains and water in saturated soils- separately by means of different sets of material points. Each Lagrangian point only carries information of the phase that represents. This MPM formulation has the capability of modeling both water within the pores and free water as a unique continuum which allows the simulation of fluid-structure interaction problems. However, the number of material points is much higher, requiring an additional computational cost. This approach has been recently adapted to the modelling of fully saturated soils [7][8].

Figure 1 shows a simplified scheme of both approaches depending on number of phases considered in a geotechnical problem. Each set of material points is represented by a circle and each color corresponds to a different phase (solid, liquid or gas).

2.2. Three-phase one-layer MPM formulation

In this lecture, the MPM formulation for unsaturated soils based on Yerro et al. [6] is outlined, as well as the explicit computational process. This is the most general “single-layer” approach because saturated and dry conditions are particular cases. Here the soil is understood as a unique medium integrated by three distinct phases (solid (*s*), liquid (*l*) and gas (*g*)) (figure 2). This is a dynamic formulation, in which all acceleration terms are considered.

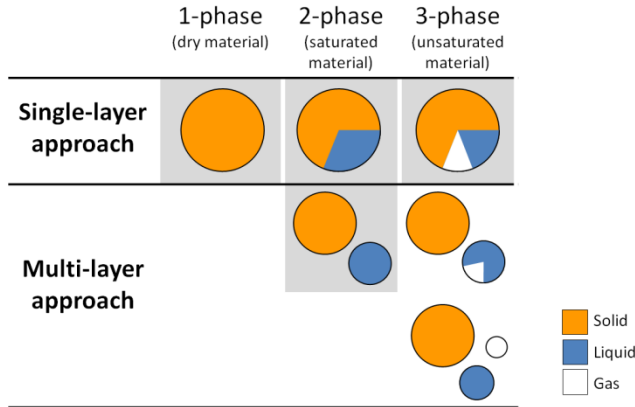


Figure 1. MPM approaches depending on the number of phases (solid, liquid and gas). Schemes colored in grey are those formulations that exist in the literature.

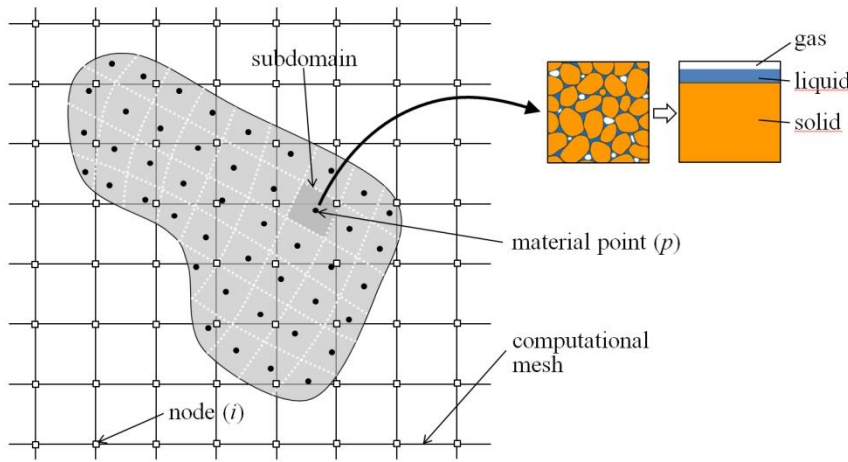


Figure 2. Spatial discretization scheme of the single-layer MPM approach for unsaturated porous material.

The main governing equations are the dynamic equilibrium of the gas, the liquid and the mixture. These are integrated into the volume and established at the nodes of the mesh at time t . At the beginning of each time step, information carried by material points is mapped to the computational mesh in order to calculate nodal mass matrixes (\mathbf{M}_l , \mathbf{M}_g and \mathbf{M}_s); nodal velocities (\mathbf{v}_l , \mathbf{v}_g and \mathbf{v}_s); internal and external forces of the liquid, gas and mixture ($\mathbf{F}_l^{\text{int}}$, $\mathbf{F}_g^{\text{int}}$, \mathbf{F}^{int} , $\mathbf{F}_l^{\text{ext}}$, $\mathbf{F}_g^{\text{ext}}$ and \mathbf{F}^{ext}); and dragging matrixes (\mathbf{Q}_l , \mathbf{Q}_g). It leads to the following system of equations (1), (2) and (3) in which liquid, gas and solid nodal accelerations (\mathbf{a}_l , \mathbf{a}_g , and \mathbf{a}_s) are taken as the unknowns of the problem.

$$\mathbf{M}_l \cdot \mathbf{a}_l = \mathbf{F}_l^{\text{ext}} - \mathbf{F}_l^{\text{int}} - \mathbf{Q}_l \cdot (\mathbf{v}_l - \mathbf{v}_s) \tag{1}$$

$$\mathbf{M}_g \cdot \mathbf{a}_g = \mathbf{F}_g^{\text{ext}} - \mathbf{F}_g^{\text{int}} - \mathbf{Q}_g \cdot (\mathbf{v}_g - \mathbf{v}_s) \tag{2}$$

$$\mathbf{M}_s \cdot \mathbf{a}_s + \mathbf{M}_l \cdot \mathbf{a}_l + \mathbf{M}_g \cdot \mathbf{a}_g = \mathbf{F}^{\text{ext}} - \mathbf{F}^{\text{int}} \tag{3}$$

Once the nodal accelerations are calculated, an explicit Euler scheme is used to update velocities, displacements and strains in the material points by means of shape functions.

Afterwards, the following mass balance equations for the solid, liquid and gas ((4), (5) and (6) respectively) are posed also in the material points; where n is the porosity, S_l is the degree of saturation and ρ_s , ρ_l and ρ_g are solid, liquid and gas densities.

$$\frac{\partial}{\partial t}((1-n)\rho_s) + \nabla \cdot ((1-n)\rho_s \mathbf{v}_s) = 0 \tag{4}$$

$$\frac{\partial}{\partial t}(nS_l\rho_l) + \nabla \cdot (nS_l\rho_l\mathbf{v}_l) = 0 \quad (5)$$

$$\frac{\partial}{\partial t}(n(1-S_l)\rho_g) + \nabla \cdot (n(1-S_l)\rho_g\mathbf{v}_g) = 0 \quad (6)$$

Considering the solid grains to be incompressible, the mass balance of solid (4) becomes the material derivative of the porosity as follows.

$$\frac{Dn}{Dt} = (1-n)\nabla \cdot \mathbf{v}_s \quad (7)$$

Including (7) in (5) and (6) and assuming that liquid and gas pressures (P_l and P_g) are the state variables, the following expressions (8) and (9) are obtained. These provide the relationships to find liquid and gas pressure rates (dP_l and dP_g).

$$n\frac{\partial(\rho_l S_l)}{\partial P_l}dP_l + n\frac{\partial(\rho_l S_l)}{\partial P_g}dP_g = \nabla \cdot [nS_l\rho_l(\mathbf{v}_l - \mathbf{v}_s)] - nS_l\rho_l\nabla \cdot \mathbf{v}_s \quad (8)$$

$$n\frac{\partial(\rho_g(1-S_l))}{\partial P_l}dP_l + n\frac{\partial(\rho_g(1-S_l))}{\partial P_g}dP_g = \nabla \cdot [n(1-S_l)\rho_g(\mathbf{v}_g - \mathbf{v}_s)] - n(1-S_l)\rho_g\nabla \cdot \mathbf{v}_s \quad (9)$$

The general method is formulated in two stress variables: net stress tensor $\bar{\boldsymbol{\sigma}}$ and isotropic suction (s). These are written in the following convenient manner (10) and (11) respectively. $\boldsymbol{\sigma}$ is the total stress tensor and \mathbf{I} is the identity matrix. It is important to highlight that when a saturated calculation is carried out, net stress defined as (10) coincides with Bishop's effective stress, which is consistent with the for saturated conditions.

$$\bar{\boldsymbol{\sigma}} = \boldsymbol{\sigma} - \max\{P_g, P_l\}\mathbf{I} \quad (10)$$

$$s = \max\{P_g - P_l, 0\} \quad (11)$$

The general form of a suitable stress-strain relationship can be written incrementally as follows, where $\Delta\boldsymbol{\varepsilon}$ is the strain increment vector. \mathbf{D} and \mathbf{h} are, respectively, the tangent matrix and a constitutive vector that depends on the constitutive model used in the problem.

$$\Delta\bar{\boldsymbol{\sigma}} = \mathbf{D} \cdot \Delta\boldsymbol{\varepsilon} + \mathbf{h}\Delta s \quad (12)$$

At the end the computational cycle associated to a time step increment, the stress and also other soil properties are updated at material point; for instance, the degree of saturation -with the corresponding retention curve-, as well as intrinsic permeabilities and porosity.

Finally, the material points carry all the updated information, the computational grid is initialized and time is updated as

$$t = t + \Delta t \quad (13)$$

2.3. Suction-dependent constitutive model

In unsaturated conditions, the stability of a slope is essentially governed by the evolution of apparent strength with the evolving suction. Several authors examined the shear strength of unsaturated soils [9][10] and observed that friction angle and especially cohesion depend nonlinearly on suction.

A suction-dependent model is presented here [6]. The shear strength is written according to the well-known Mohr-Coulomb elastoplastic criterion. In order to include the suction effect, both strength parameters (cohesion c and friction angle φ) can be generally written as the sum of two terms as follows:

$$c = c' + c_s \quad (14)$$

$$\varphi = \varphi' + \varphi_s \quad (15)$$

where c' and φ' are the values for saturated conditions (effective cohesion and effective friction angle), whereas c_s and φ_s depend on the level of suction and provide an apparent strength.

It has been accepted that cohesion can increase from c' up to $c' + \Delta c_{\max}$ according to (16). P_{atm} is the atmospheric pressure and B is a constant parameter that controls the rate of apparent cohesion. Although changes in internal friction angle are typically less relevant, it is considered that it has linear dependence with suction depending on A .

$$c_s = \Delta c_{\max} \left(1 - e^{-B(s/P_{\text{atm}})}\right) \quad (16)$$

$$\varphi_s = A(s / P_{\text{atm}}) \quad (17)$$

2.4. Strain softening constitutive model

A strain weakening behavior is typically exhibited by rocks and overconsolidated clays. This is characterized by a reduction of the material strength from peak to residual conditions expressed as function of shear strains. The change of strength in the most loaded points of the slope causes a redistribution of the stresses. This fact may lead to more neighboring points reaching the maximum strength inducing a progression of the failure surface. Because of that, in this kind of materials a shear band does not occur simultaneously along the entire rupture surface, but shear strains localize gradually until a kinematically admissible mechanism is developed.

In order to simulate the complexity of the behavior of brittle materials, a strain softening Mohr-Coulomb model is implemented [11]. Softening behavior is accounted for by reducing the strength parameters (effective friction angle φ' , and effective cohesion c') with accumulated deviatoric plastic strain invariant ε_d^p according to the following softening rules:

$$c' = c'_r + (c'_p - c'_r) e^{-\eta \varepsilon_{eq}^p} \quad (18)$$

$$\varphi' = \varphi'_r + (\varphi'_p - \varphi'_r) e^{-\eta \varepsilon_{eq}^p} \quad (19)$$

The model requires the specification of peak (c'_p, φ'_p) and residual (c'_r, φ'_r) strength parameters. The rate of strength decrease is essentially controlled by the plastic shear strain but an additional “shape factor” parameter η is also included in equations (18) and (19). The higher the shape factor η , the smaller the loss in strength.

3. First failure in brittle materials

First failures may be induced by different external actions. In man-made failures excavation of cuts (unloading) or the increase in loads may lead to failure. When examined in detail, some well-known cases of brittle failures (Aznalcóllar dam [12]; Selborne failure experiment [13]) are a combination of shear stressing and also a change in total stresses and pore pressures.

Soil brittleness leads to a progressive failure phenomenon. This process, conceptually independent of time, may be described as a static process in which slope deformations tend to be small because of the stiff nature of brittle clays. However, the final instability is associated with a non-equilibrated stress release and therefore with an accelerated motion. The subsequent motion is controlled by Newton law and the consequences of the instability depend on additional aspects, typically related to the geometry of the site at a larger scale. The case of Selborne will be analyzed here to illustrate these aspects.

The Selborne cut was excavated in Gault clay (weathered in the upper 7–8 m). Figure 3a shows a representative cross section. Two lateral trenches, 25 m apart, were excavated to eliminate restrictions to a failure experiment conceived as a two-dimensional case. The instability was induced by

increasing the pore water pressure in a series of boreholes drilled from the upper subhorizontal surface of the slope. In the simulation performed, the pore water pressure increase was simulated by means of a boundary increase in water pressure.

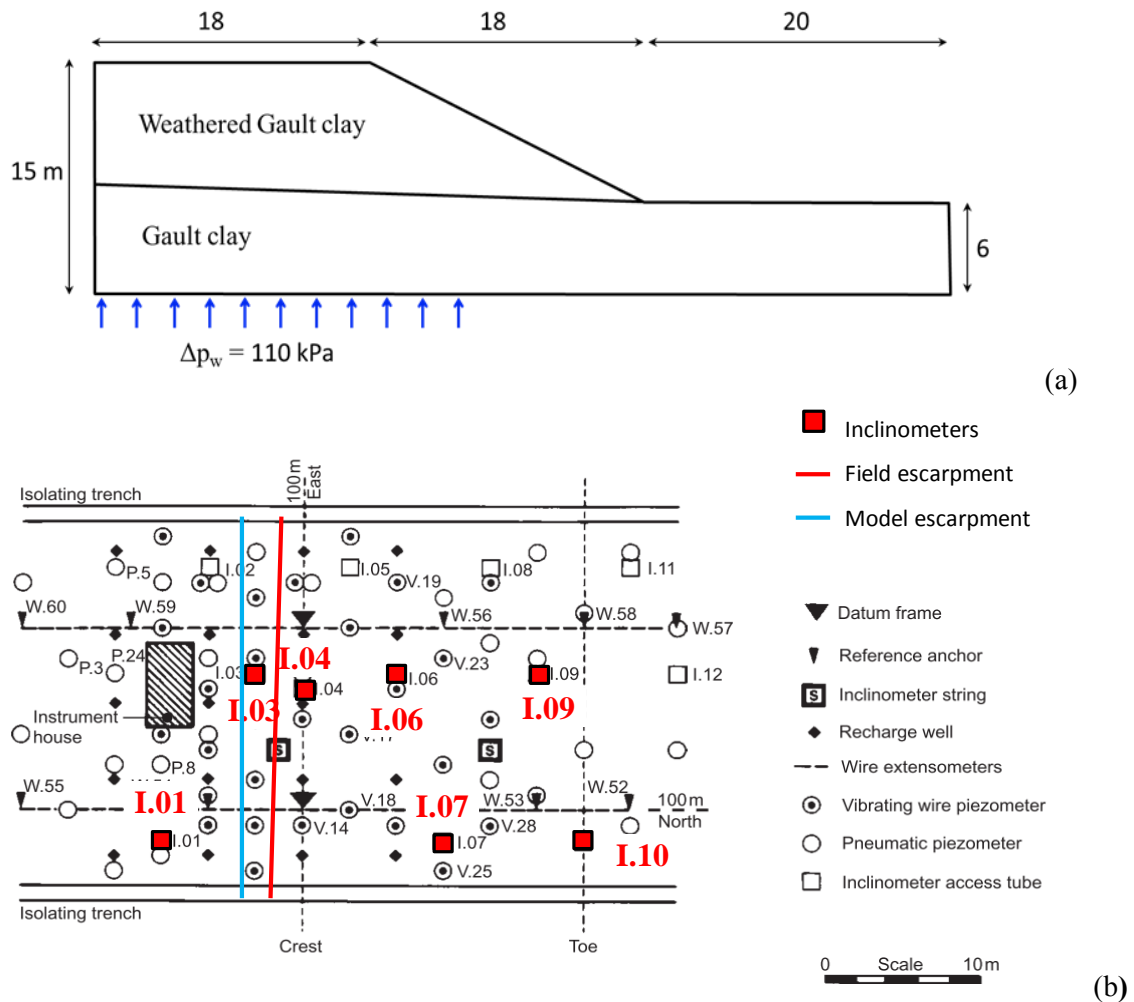


Figure 3. (a) Representative cross section of Selborne failure experiment; (b) Plan view of position of monitoring instruments [13]

The slope was monitored by means of surface topographic marks, piezometers and inclinometers. A detail of their position is given in plain view in figure 3b. The main Gault clay properties adopted in the analysis performed were collected in table 1. Porosity, unit weights, elastic parameters and effective strength parameters are derived from laboratory tests reported in Cooper et al. [13]. The clay permeability was artificially increased to reduce the computational time. In fact, the explicit formulation of the MPM analysis requires very small time increments. However, field and computational times may be compared in dimensionless terms: $t^* = t/T$, where t is the real time and T the time to failure.

Note in table 1 that the stiffness and strength properties of the weathered and unweathered clay are very similar.

The computational mesh as well as the initial location of material points is shown in figure 4. Elements are 3D tetrahedral elements. A plane strain “slice” of the slope was simulated. The density of material points was increased in a region when slope deformations are expected. The average size of

tetrahedral elements was selected in connection with the strain softening “shape factor” parameter, η , of the clay constitutive model. Figure 5 shows the effect of varying η and the mesh size on the predicted displacement of the crest point of the slide. An element size of 0.7m and $\eta = 400$ was selected.

The initial stress state in the model was due to gravity effects. The excavation process was not simulated in the set of results described below. This is admittedly a limitation because of the relatively high K_o value expected in these overconsolidated clays ($K_o \cong 1.5$ to 2). However, this aspect is being currently investigated in more detail.

Table 1. Properties of Gault clay.

	Weathered Gault clay	Gault clay
Porosity	0.2	0.2
Permeability (m/s)	0.001	0.001
Dry unit weight (kN/m ³)	2,500	2,500
Young modulus (kPa)	20,000	20,000
Poisson's coefficient	0.33	0.33
Effective cohesion (peak/residual)(kPa)	13/4.7	25/1
Friction angle (peak/residual)(°)	24.5/13.5	26/15
Calibration parameter, η	500	500

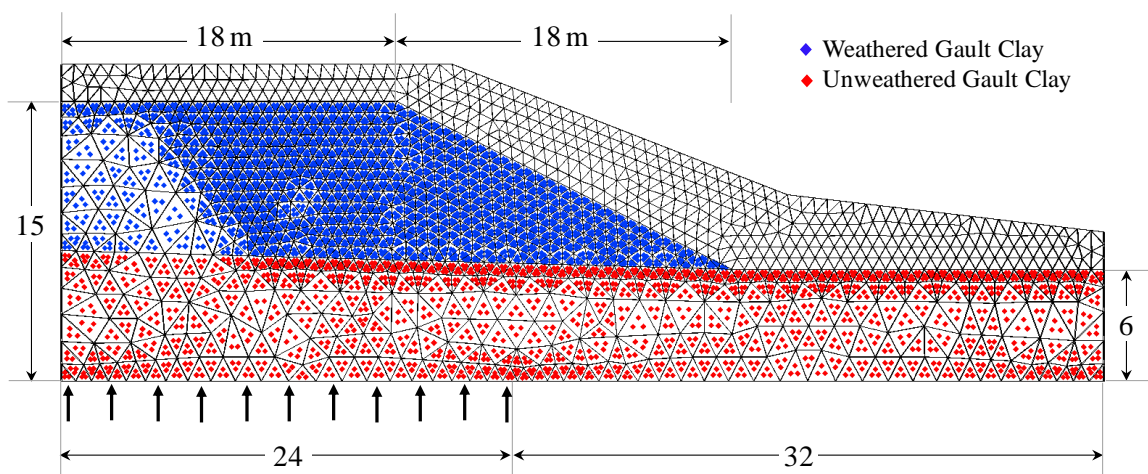


Figure 4. Computational mesh for the Selborne failure experiment

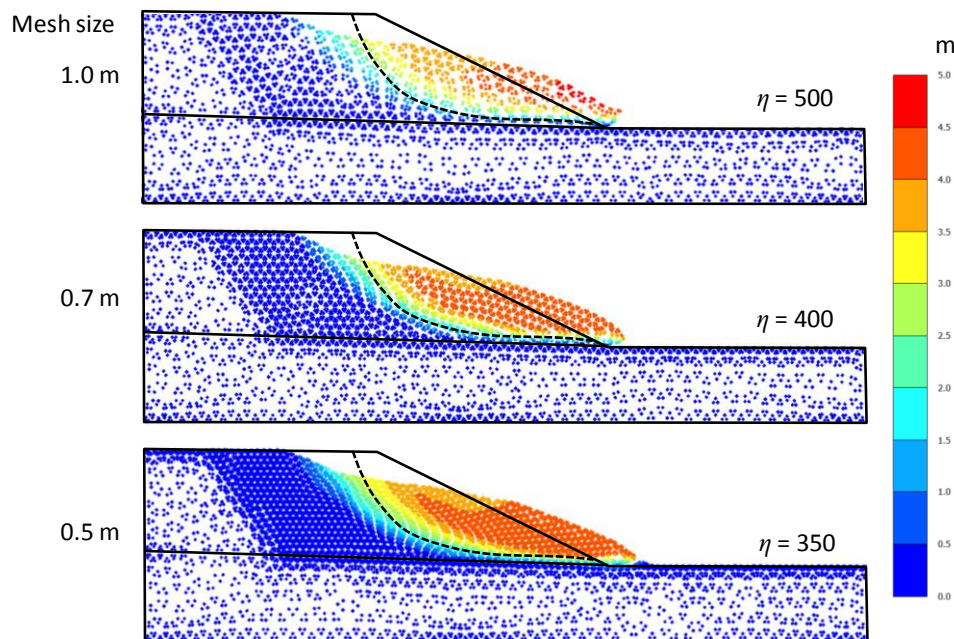


Figure 5. Effect of mesh size and the shape factor parameter on displacement pattern at failure.

3.1. Model calculations and slope response

Selborne is an interesting case because there is data available on the evolution of pore pressures and inclinometer readings during the hydraulic loading of the slope. In addition, the motion of the slide after failure was reported in Grant [14]. This information is particularly valuable to check the capability of the dynamic MPM model to capture the slide run-out, a piece of information that is generally absent in Limit Equilibrium and Finite Element analysis.

Pore pressures were recorded in a high number of sensors. Three records, selected for their proximity to the actual failure surface, are compared with model calculations in figure 6. The agreement is quite reasonable. Records for points B and C show a rapid decrease in pore pressure in the proximity of the final failure. This is probably due to the combined effect of positive shear-straining induced dilation and the unloading associated with the slope motion. However, a zero dilatancy angle was used in the analysis.

Post-failure displacements on two parallel lines to the sliding direction are shown in figure 7. The slide moved towards the East. Therefore, the two reference lines are indicated as North and South. The distance between them is around 17m. Calculated results are especially accurate for the Northern part. The maximum recorded motion of central points of the slope was about 4m. The MPM model reproduced correctly the kinematics of the motion. The smaller displacement of the Northern side was attributed by Cooper et al. [13] to an overall rotation of the slide, towards the North that introduced an additional restraining force in the Northern side of the slide. The figure shows also the MPM calculated deformed shape of the slope. It corresponds to an effective cohesion of 4.7kPa, which is a small value. It was found that the slide displacement was quite sensitive to the value of c' , even if it is small (with reference to the usual understanding of small cohesion values in engineering practice). This sensitivity is illustrated in figure 8a. It shows the variation of the displacement of the crest point with residual cohesion. The value $c' = 4.7\text{kPa}$ was justified because of the suction measured in a few piezometers located in the lower part of the slide. This suction varied between 0 and 40kPa. A mean value of 20kPa and a residual friction of 13.5° lead to a suction-induced apparent cohesion of 4.7kPa (the clay remains most probably saturated for the small range of measured suctions).

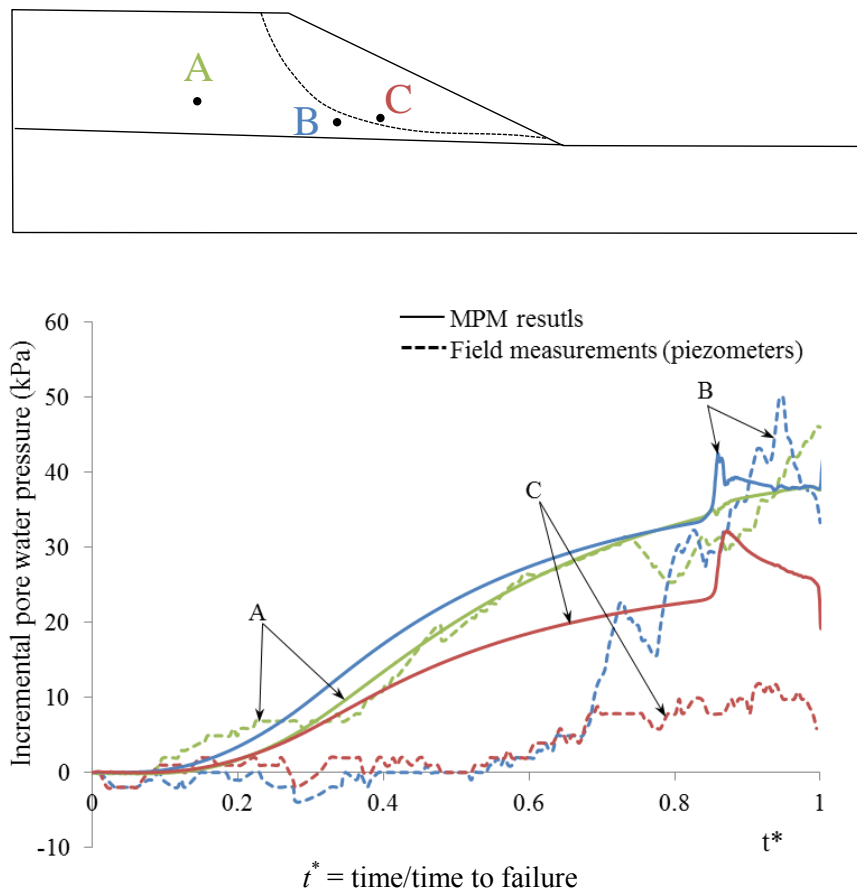


Figure 6. Piezometer records and model calculations.

Also indicated in figure 8b is the effect of time step in slide displacement. A “safe” value of $\Delta t = 1.3 \times 10^{-4}$ s was used in calculations.

The geometry of the initial sliding surface was also recorded. It is compared with MPM calculations in figure 9. The predicted shape follows the maximum values of plastic deviatoric strains immediately before final failure. The model captures correctly the surface shape and the dominant effect of the contact between weathered and unweathered Gault clay. The actual failure surface was however somewhat shallower than the predicted one.

Inclinometer readings allow also a further set of data to check the validity of the model. Readings for inclinometers located on the excavated slope (I04, I06, I07 and I09; see figure 3.1b) are compared with model calculations in figure 10. Predicted displacements for two times close to the failure time are given. They approximate the time of inclinometer readings before the final run-out time. Note the scale of the horizontal displacements, which belong to the quasi-static, pre-failure stage of the slide. The calculation’s results bound the actual measurements. The patterns of displacements are also reasonably well captured by the model and show the position of the failure surface.

The progressive failure was qualitatively described by Cooper [15] by interpreting inclinometer data. It was accepted that the toe of the slope was in residual conditions at the beginning of the experiment as a result of the previous excavation.

The shearing band progressed simultaneously in opposite directions from the higher and lower levels of the final position of the sliding surface. The band propagated towards the center part.

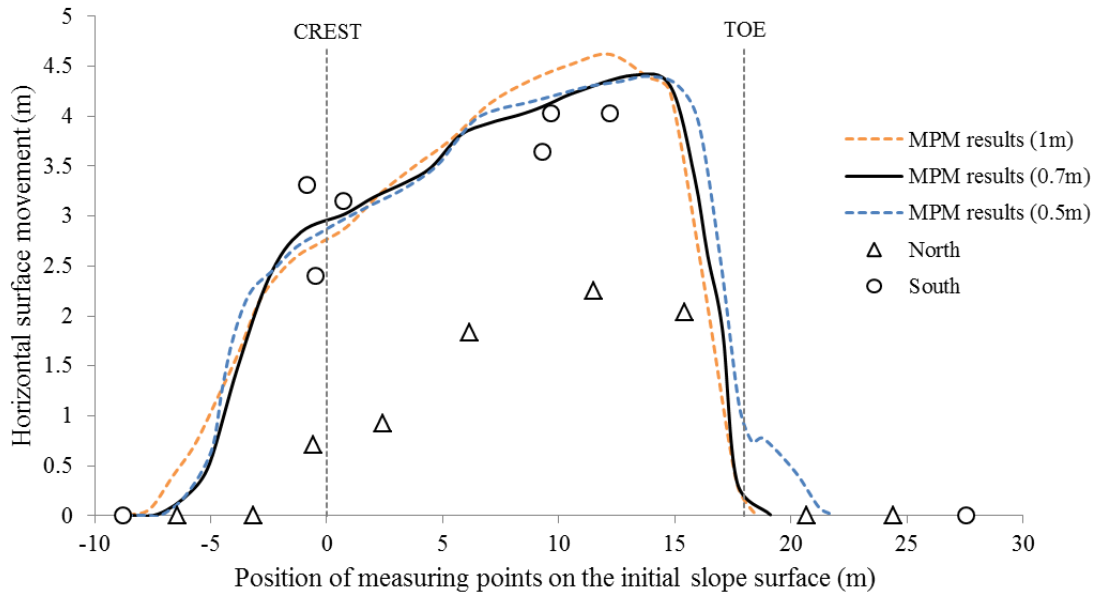


Figure 7. Measured and calculated displacements after failure.

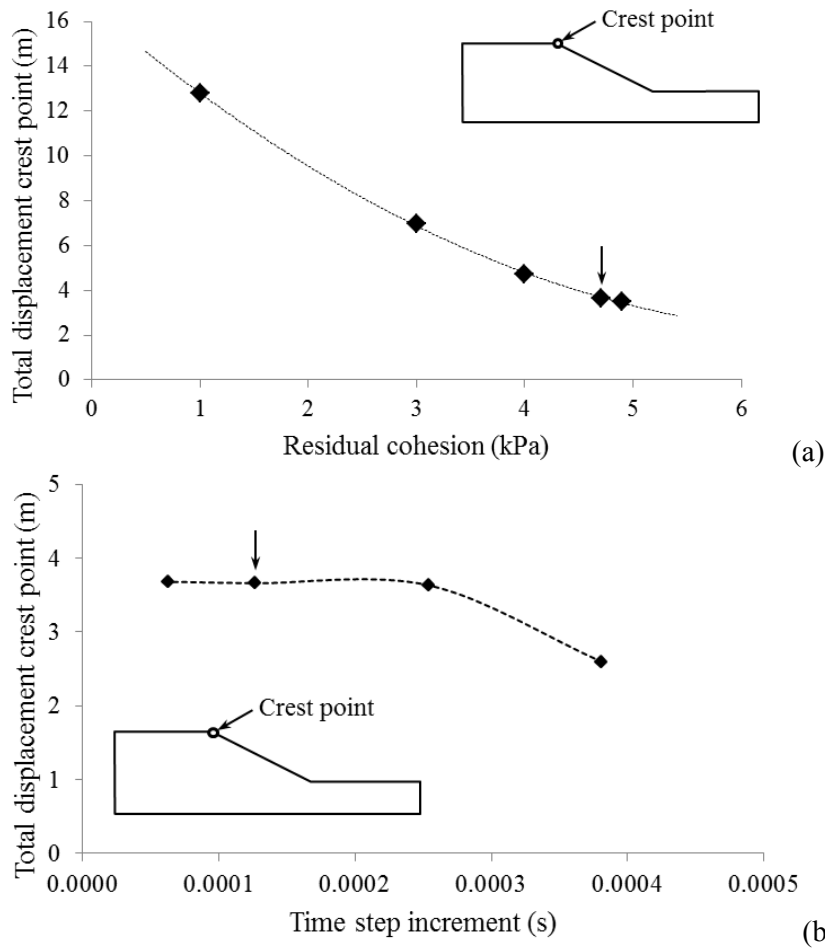


Figure 8. Total displacement of crest point after failure (a) Effect of residual cohesion strength; (b) Effect of calculation time step.

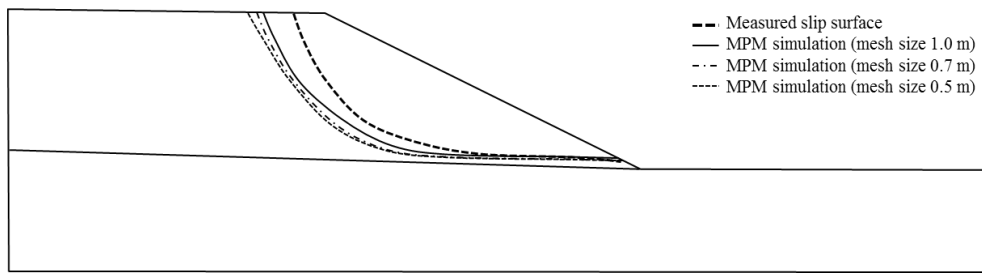


Figure 9. Comparison between measured and predicted shape of failure surface.

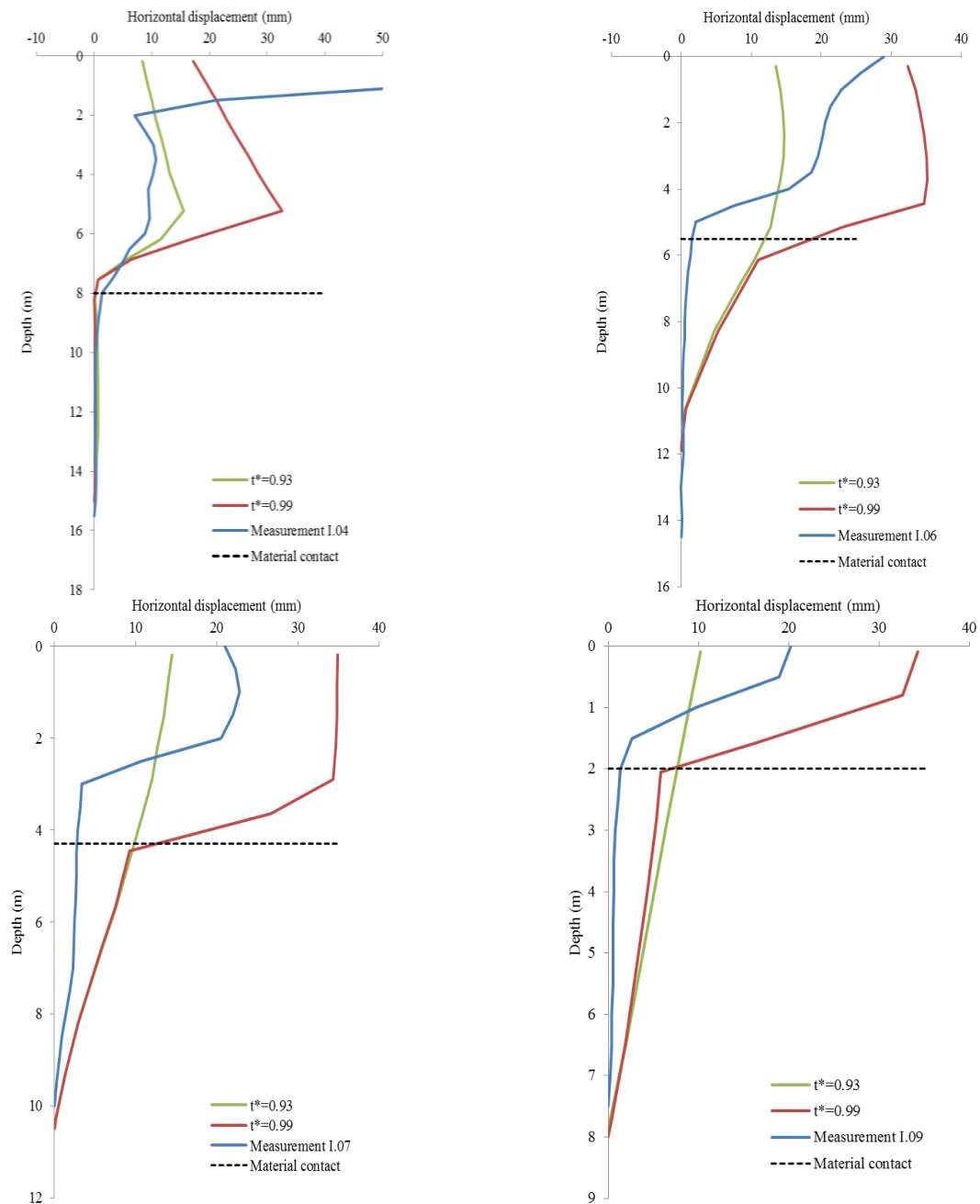


Figure 10. Measured and predicted inclinometer readings.

The model offers the opportunity to examine this result in some detail. A mobilized friction angle was defined as

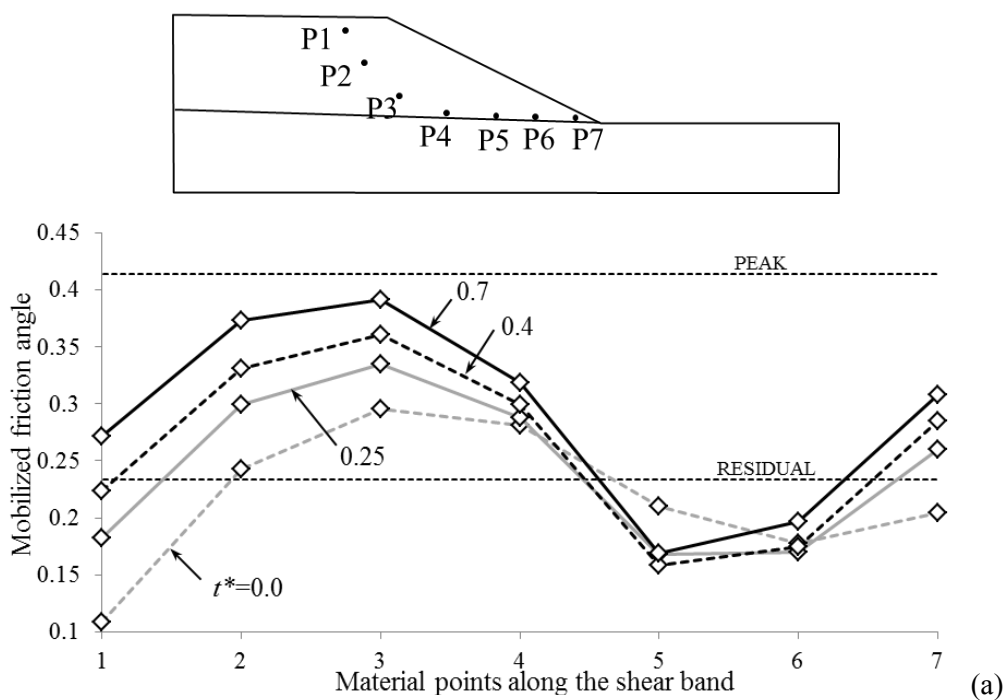
$$\sin \hat{\phi}' = \frac{q}{p^*} \quad \text{where } p^* = p' + \frac{c'}{\tan \phi'} \tag{20}$$

q and p' are the deviatoric and mean effective stresses. Plots of $\sin \hat{\phi}'$ along the (final) shear surface for different dimensionless times are given in figure 11a,b,c.

Early times are given in figure 11a. Initially ($t^* = 0$) the slope remains in elastic conditions.

Maximum shear stresses are calculated at mid and upper heights (positions P2 and P3). As the water pressure increases the mobilization of shear strength continues in the upper and lower parts of the sliding surface. The first yielding (peak conditions) occur at $t^* = 0.83$ at P2. This is followed by a generalized plastification of the upper stretches of the failure surface which rapidly reach residual conditions at $t^* = 0.84$ and 0.845. Interestingly, this is immediately followed by the plastification of the toe of the slope (at $t^* = 0.85$). The evolution of shear stressing at later times, close to the failure is shown in figure 11c. The plastification advances in opposite directions from upper and lower parts, and the final point resisting under peak conditions is P4. This was also the inference based on inclinometer results.

The evolution of progressive failure in terms of an average friction angle can be followed in figure 12. The mean friction angle increases continuously until peak strength conditions are reached for the first time at a point around P2 for $t^* = 0.83$. Immediately afterwards there is a drop of available mobilized strength. Then the process of progressive failure progresses at essentially constant average mobilized strength. This process ends abruptly when the final point in the failure surface to reach peak conditions evolves towards a residual state. This sudden final drop of mobilized strength marks the beginning of an accelerated motion. The average (p', q) points at the three critical instants mentioned are plotted in figure 12b in a triaxial stress space.



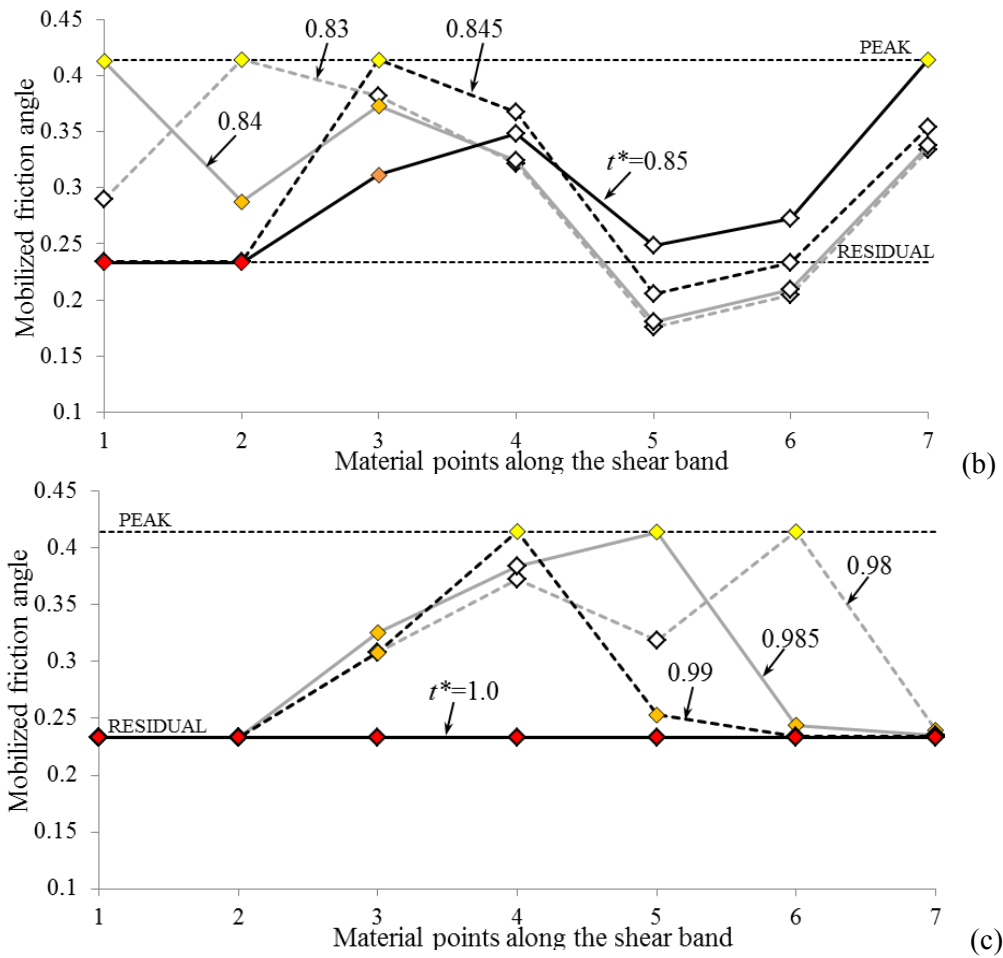
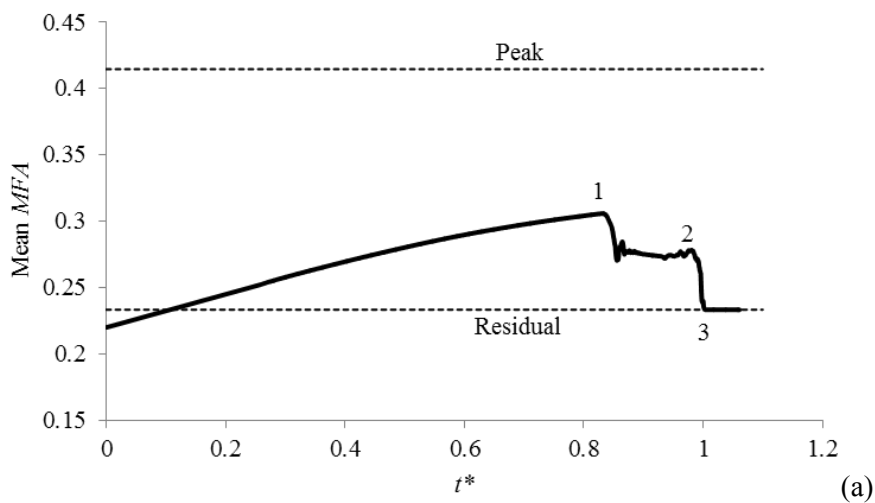


Figure 11. Development of progressive failure at (a): Early times; (b) Intermediate times; (c) Final times. The colour of the markers indicate the state of the point (white: elastic; yellow: peak conditions; orange: under softening; red: residual conditions).



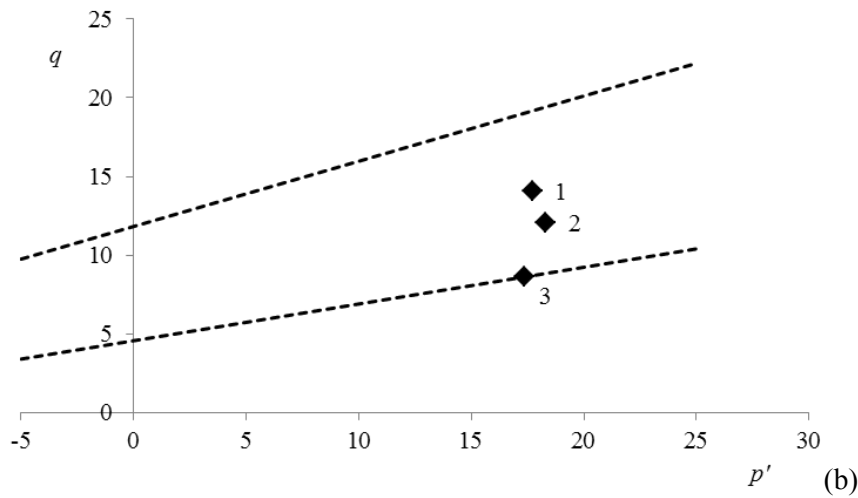


Figure 12. Evolution of (a) mobilized friction angle and (b) average (p' , q) stress points.

The motion of the slide is summarized in figure 13. Velocity, displacement and acceleration of four points in the slope (C1 to C4) are plotted in terms of dimensionless time. Maximum velocities and displacements are calculated for points in the upper central part of the sliding mass. The maximum calculated velocity is close to 0.9m/s. The maximum calculated acceleration is a small fraction of gravity acceleration (0.036g).

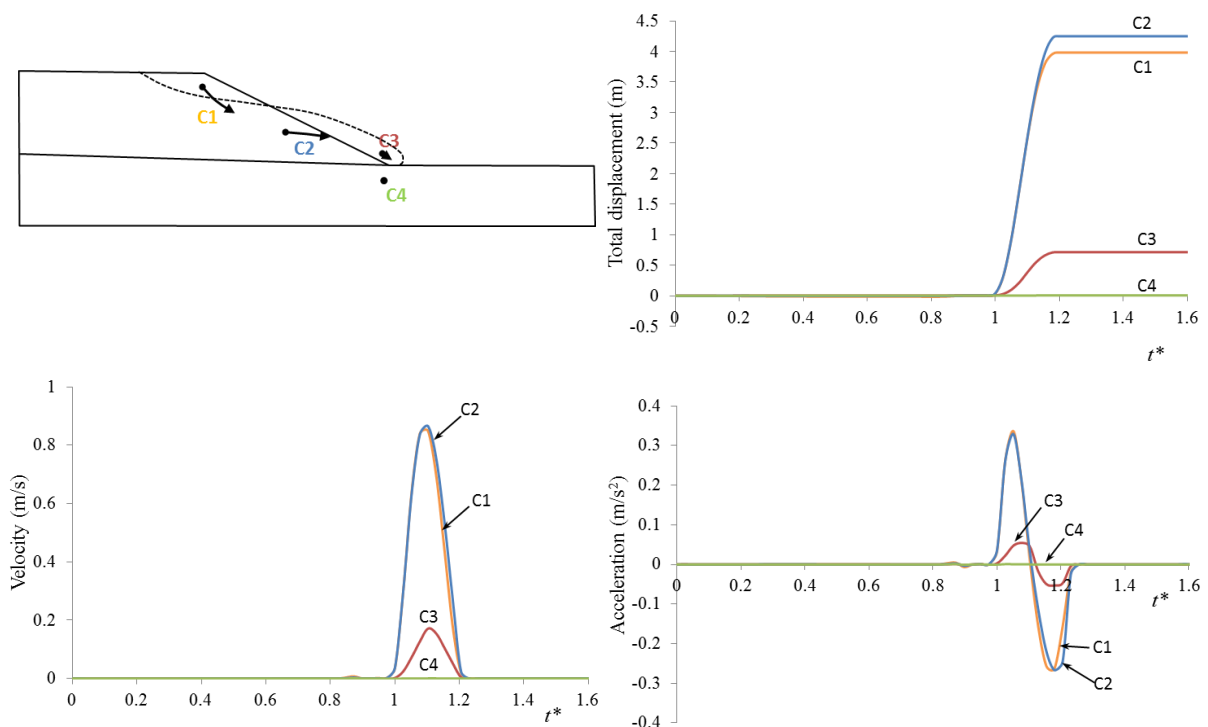


Figure 13. Kinematics of the motion: Total displacements, velocity and acceleration of four representative points of the slide.

Figure 14 relates the mobilized friction angle of three points on the sliding surface with the development of the accelerated motion. The sudden drop of (average) friction beyond the attainment of peak conditions for the first time is well identified as well as the final reduction of available

mobilized strength and the associated acceleration of the sliding mass. Changes in geometry during sliding are reflected in small changes in mobilized friction due to some local unloading. The small arrows in figure 14 indicate the times selected in figure 11 to show the distribution of mobilized strength along the sliding surface.

A further illustration of the processes taking place inside the slope is given in figure 15. It shows the stress paths of two points: P2 in the upper part of the sliding surface and C4 at the toe of the slope, below the sliding surface. Point P2 is initially (A) in an elastic state. The progressive increase in pore pressure takes the point to peak strength conditions at a reduced mean effective stress. The small increase in q is associated with the effect of boundary water pressure applied only on part of the lower boundary. The sudden increase in q before reaching peak strength conditions is probably a result of internal stress changes due to the unloading of points reaching peak conditions. Beyond point B the continuing increase in pore pressure reduces the effective mean stress and, in parallel, the strength reduces progressively to residual conditions. The Mohr-Coulomb model used has not a cut-off, tensile strength and p' may become negative. Changes in pore pressure when the progressive failure begins to operate were also calculated and represented in figure 6 (beyond $t^* = 0.83$). The increase in pore pressure may be due to total stress changes induced by the sudden release of stresses along the failure surface. Reduction in pore pressure is explained by the flow/consolidation phenomenon and the boundary conditions. The end result is a cycle of increase/decrease of pore pressures, which is well identified in figure 6 but also in figure 15 for point P2 when the stress path moves along the residual strength envelope and reaches a final state at point C.

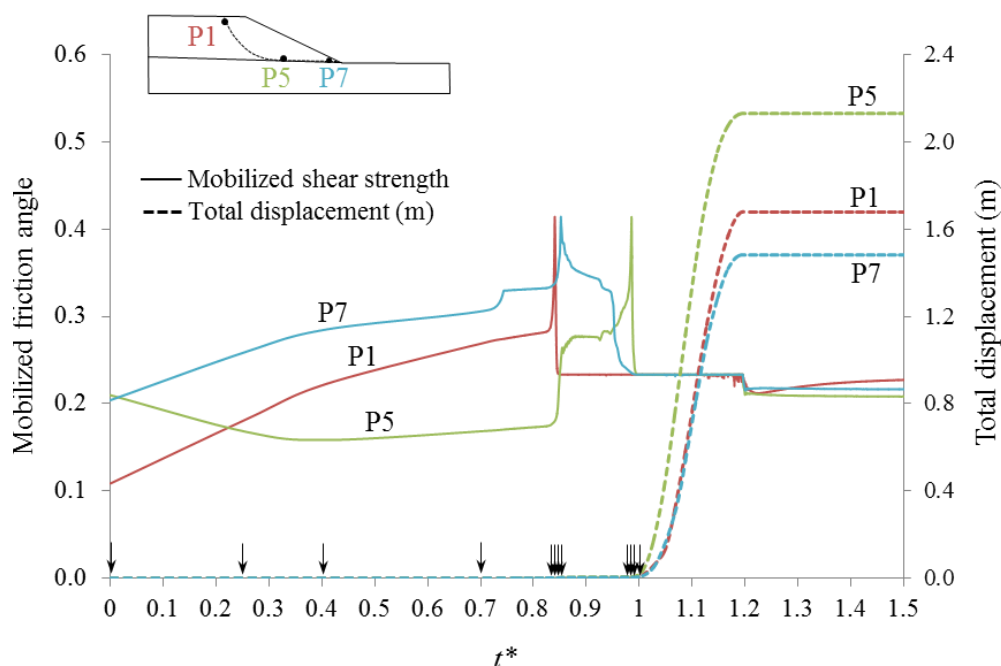


Figure 14. Evolution in time of mobilized friction angle and slope displacements before and after failure for points P1, P5 and P7.

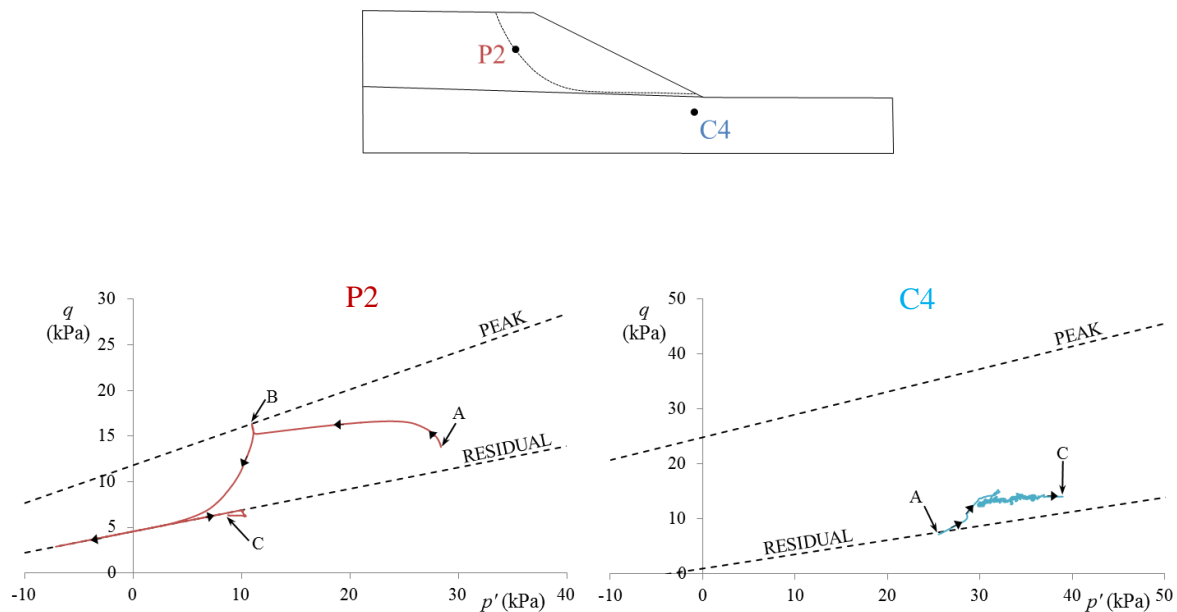


Figure 15. Stress paths in material points P2 and C4.

Point C4 behaves in a simpler way. The point, slightly affected by the instability, remains in an elastic condition throughout the test. The increase in mean effective stress is a consequence of the changes in slope geometry (mass of soil accumulating at the toe). Pore pressures are not expected to change in C4.

3.2. Lessons from the modelling of Selborne experiment

The Selborne failure experiment remains as one of the most informative field experiences to illustrate the nature of progressive failure in overconsolidated brittle, high plasticity clays. The interest of the case increases because of the available information on post-failure behavior. Therefore, an opportunity exists to perform an integrated analysis of pre and post-failure slope behavior. Validating such an experiment, which was preceded by a good identification of laboratory-based soil properties, provides an interesting support to the analysis performed. The “static” part of the analysis described is in itself a valuable addition to the interpretation of field measurements.

Some relevant points of the review of the pre-failure part of the experiment are:

- The identification of the progressive failure mechanism, which progresses from the two extremes of the failure surface towards the central part of the sliding surface.
- The quantitative evolution of the mobilized average shear strength that shows two distinct critical moments: the first arrival to peak strength and the last one. In between, the average mobilized strength is essentially constant. The final sudden drop in average mobilized strength triggers the accelerated slide motion.

The “availability” of field displacements after failure allowed a further check of the model. The calculated displacement pattern agreed well with actual measurements. However, the result is highly dependent on the adopted residual effective cohesion. Small changes of this strength parameter (justified in the Selborne case by the occurrence of “in situ” suctions) result in significant changes of run-out results.

One limitation of the analysis refers to the effect of the initial excavation, which was not considered. This is expected to modify to some degree the initial stress state. A second difficulty is the very long computational time for the explicit code in cases of low permeability. However, results plotted in terms of relative time with respect to the failure time seem to be consistent with field data.

4. Deep seated fast landslides

“Compound” landslides, a classification category included in the recent review of Hungr et al. [16], are a relatively common class of motions, which require internal shearing to accommodate the kinematics of the motion. In deep seated landslides internal shearing will affect long distances in rock masses that, as a rule, are brittle materials. Therefore, (a) the stability of the landslide will be, to a large extent, controlled by internal shearing; (b) progressive failure mechanisms are expected during the deformation of the slide and (c) a final accelerated motion will be a consequence of the release of energy once static equilibrium is lost.

The sliding surface, on the other hand, may have a completely different character, especially in the case of reactivated slides. Often the basal sliding plane follows a weak layer, typically a claystone in a sequence of stiffer levels. If high plasticity minerals dominate the weak clayey rock very low residual friction angles (and no cohesion) will be operating on the basal failure surface. In these cases, the internal shearing through competent but brittle rocks should play a major role to explain stability conditions but also to control the post-failure behaviour.

This section investigates the static and dynamic behaviour of a landslide characterized by the previous description. An archetypical case is Vaiont landslide, which has been simplified in some cases [25] as two interacting wedges through a common shearing plane, which is necessary to accommodate the kinematics of the motion if no gaps between the moving mass and the basal sliding plane are accepted. However, there are infinite possibilities to build an admissible deformation pattern. In fact, the kinematic mechanism is part of the solution of the problem and not a necessary previous assumption. One of the objectives of this work was to find the kinematic mechanism of a given sliding geometry knowing that the rock behaves as a brittle material.

4.1. The model

Consider in figure 16 the 2D model analysed. Geometry and dimensions correspond to “section 5” of Vaiont landslide defined in Hendron & Patton [18] and Pinyol & Alonso [25]. An equilibrium state will be found for a set of strength parameters of the rock, the basal sliding surface and a given position of the water level in the reservoir, h_w .

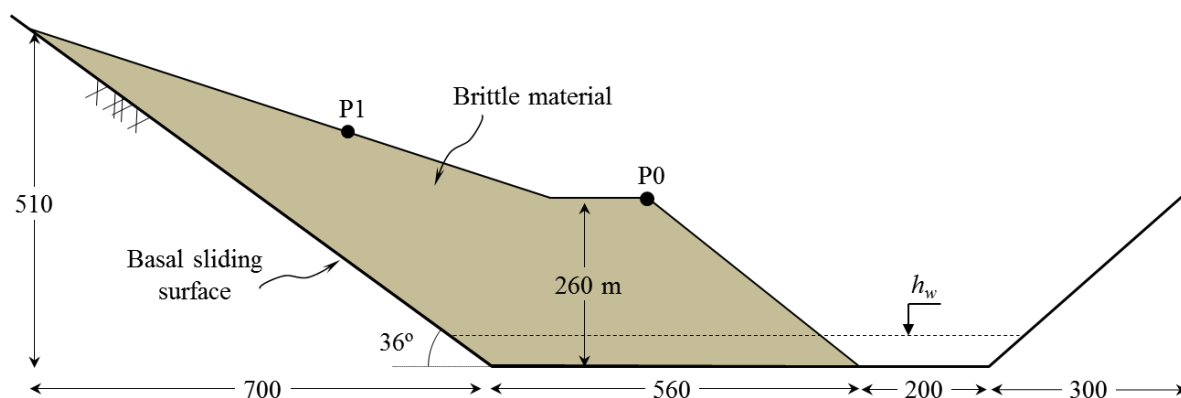


Figure 16. The analyzed landslide. Vaiont geometry.

Rock properties were derived from the analysis presented by Pinyol & Alonso [17]. A residual friction angle of 12° was adopted for the basal sliding surface following the data and discussion given by Hendron & Patton [18]. The set of material parameters is given in table 2.

Figure 17 shows the material and computational mesh. The computational mesh was extended to the right margin of Vaiont River to allow for a large displacement of the slide.

The basal sliding surface was simulated by means of a contact algorithm between the moving rock mass and a rigid lower layer, which acts as a lower boundary for the landslide.

The analysis was performed under drained conditions. At each time step, the current hydrostatic water pressure was imposed on material points. Points above the specified reservoir water level have no water pressure. Water in the reservoir was not modeled.

Table 2. Material parameters for the deep seated landslide.

Material parameter	Value
Rock porosity, n	0.2
Young Modulus, E [MPa]	5
Poisson ratio, ν	0.33
Peak effective cohesion, c'_r [kPa]	300
Peak effective friction angle, ϕ'_p	42°
Residual effective friction angle, ϕ'_r	36°
Shape factor, η	150
Basal residual friction, ϕ'_{res_0}	12°

4.2. Modelling results

The first step in the simulation was to introduce an initial stress state by activating gravity. The response of the slope to the imposed weight is shown in figure 18. The rock mass deforms slightly but the calculated deformation is enough to generate a band of plastic shearing deformations, which anticipates the kinematic mechanism in case of additional loading (increase in pore pressure). Deviatoric plastic strains reach a maximum at the kink between the two basal planes and extend upwards, almost vertically without reaching the slope surface. Strains are small but some points in the rock mass have already reached the peak strength.

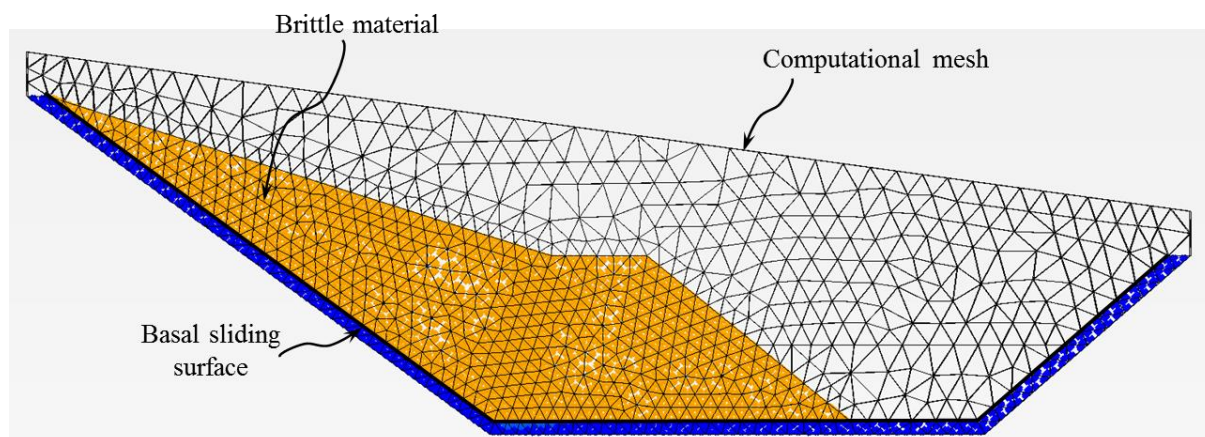


Figure 17. Computational mesh.

The next step is to increase the reservoir water level in the manner indicated in figure 19. The slide response is also shown in the figure. The internal shearing plane develops progressively (note the change in the scale of plastic shear strains). When the water level reaches 53m, a horizontal displacement of 8.5m is calculated for point P0 in figure 16.

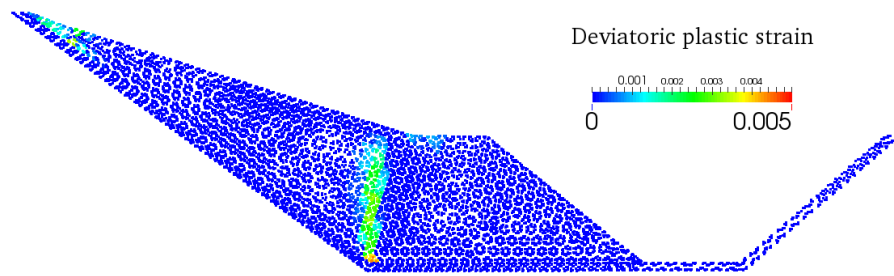


Figure 18.
 Deviatoric plastic strains after activation of gravity.

The progressive failure along the internal shear band starting at the kink point of the sliding surface is illustrated in figure 20. A mobilized friction was defined as in equation (20). Peak and residual thresholds are shown as well as the “available” strength for the initial time (t_0). This available strength is not the peak strength because it includes already the progressive failure taking place during the initial application of the gravity loading. Note that the lower points of the internal shearing plane had already suffered some amount of strength degradation. Increasing the water level mobilizes progressively upwards the friction angle. At time t_4 ($h_w = 57$ m) the entire plane is close to peak conditions and subsequent water level increments reduce the available friction to residual conditions. Note that the residual friction angle of the rock (36°) implies that a substantial shearing resistance is still being offered by the internal shearing of the rock.

The final stable geometry for $h_w = 60$ m is shown in figure 21. The drop of rock friction to residual conditions leads to an increase of the plastic shearing strains but also to a change in the inclination of the shearing plane, which is now close to the bisection of the sliding surface dihedral angle.

The calculated displacement and velocity of the slide, once this internal plane has reached residual conditions is shown in figure 22. The maximum calculated velocity is around 0.5m/s very far from the estimated maximum velocity in Vaiont (25.30m/s).

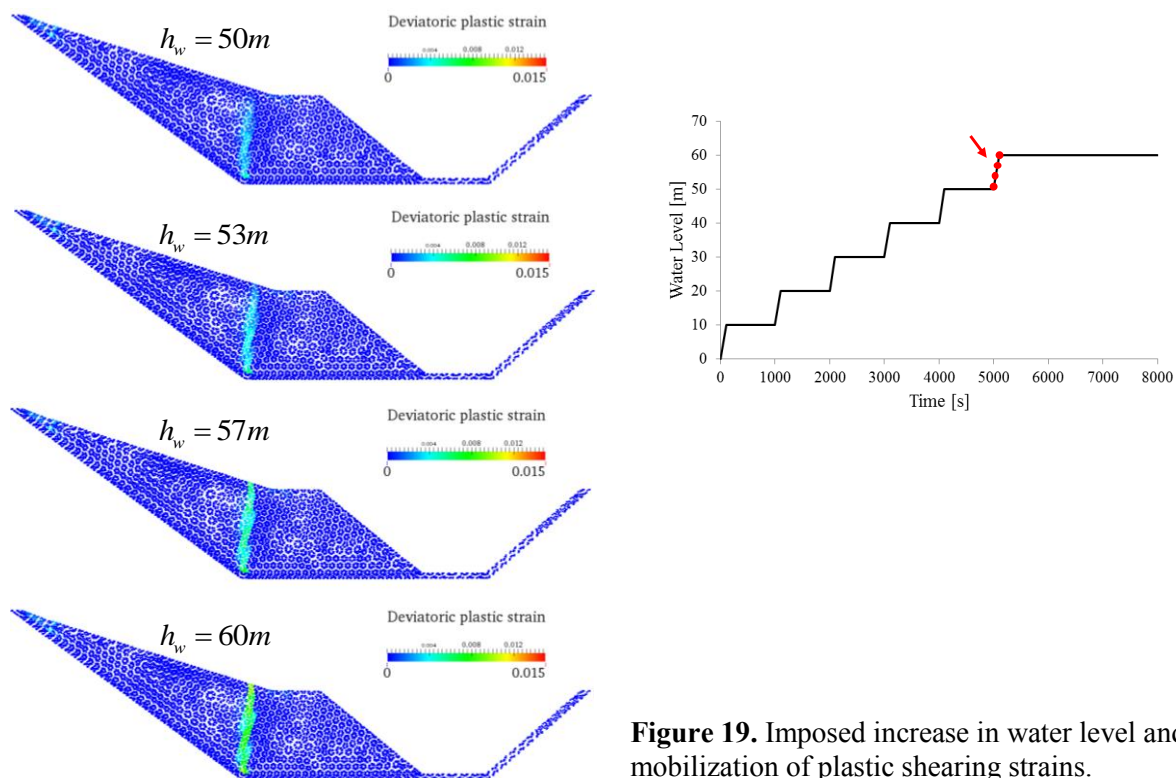


Figure 19. Imposed increase in water level and mobilization of plastic shearing strains.

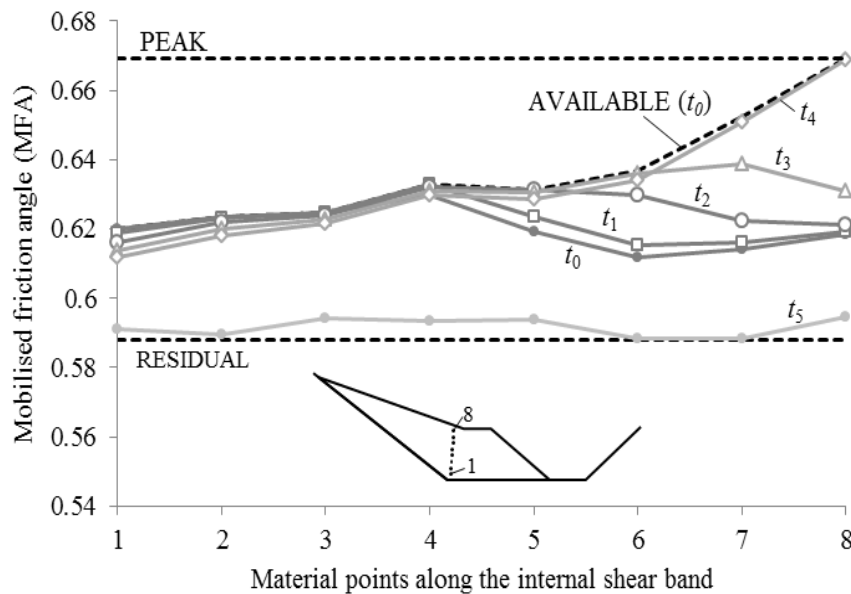


Figure 20. Mobilization of friction angle on internal shearing plane.

In order to increase significantly the run-out and the sliding velocity it is necessary to reduce the operating friction angle in the basal plane. This possibility is explained by the thermal pressurization of the basal clay layer and it has been proposed and justified by many authors [19][20][21][22][23][24]. Although some of the hypotheses change among the authors invoking the thermal pressurization, a plausible and simple explanation relies in the different thermal dilation coefficients of water and soil/rock skeleton. In practice this effect leads to a reduction in normal effective stress on the basal shearing surface. This reduction is fast and leads to an “explosive” reaction that reduces effective stress to zero (zero equivalent residual friction).

This phenomenon was simulated in the MPM by reducing the residual friction angle of the sliding surface. Two cases are graphically illustrated in figure 23: $\varphi'_{res_b} = 5^\circ$ and $\varphi'_{res_b} = 0^\circ$. The two sets of plots are similar. The slide accelerates and deforms and in the case of $\varphi'_{res_b} = 0^\circ$ it climbs up the opposite valley slope. The plot shows in a colour scale the calculated plastic deviatoric strains. Moving beyond the kink in the basal sliding surface results in a massive shearing of the rock. As new intact rock enters the position of a virtual shearing plane, plastic strains develop and the damaged rock moves forward to a new position. This process increases the volume of damaged rock in the direction of the motion. This is illustrated in figure 23. In the case of zero residual friction angle, most of the rock involved in the landslide has been damaged because of the two “kinks” of the basal surface at the two sides of the valley flat surface.

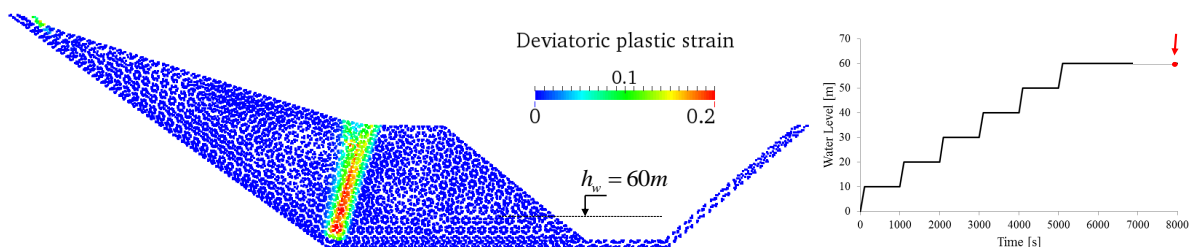


Figure 21. Stabilized geometry and development of shearing plane when $h_w = 60m$.

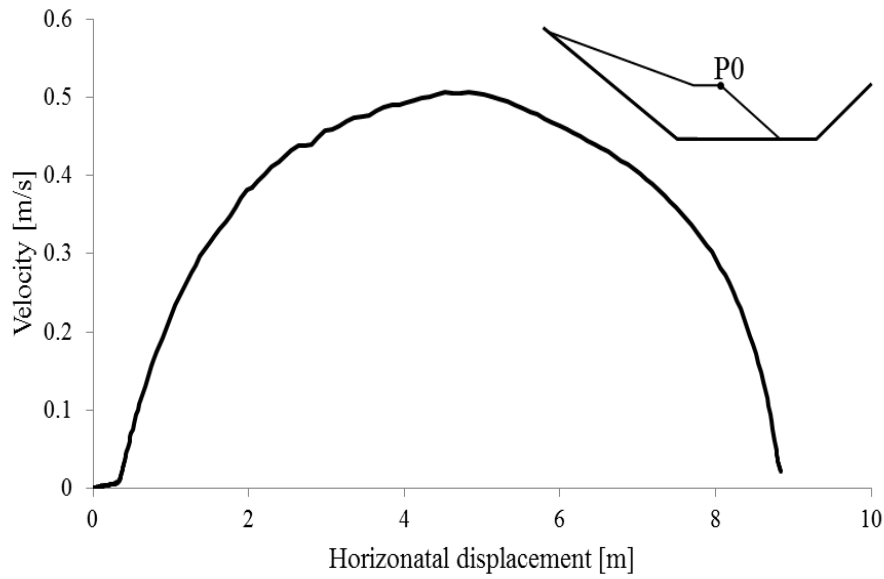


Figure 22. Velocity-displacement response of the slope for $h_w = 60\text{m}$ ($\phi'_{res_0} = 12^\circ$).

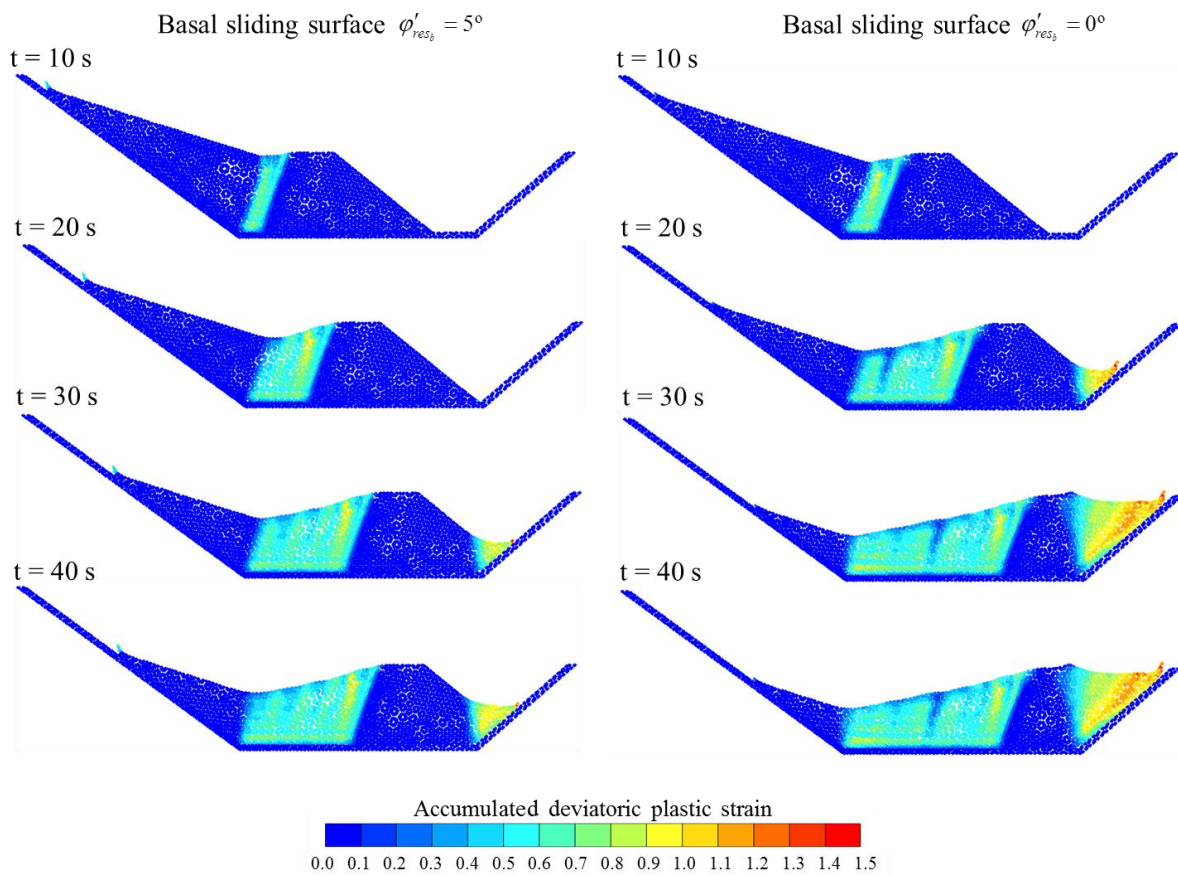


Figure 23. Evolution of landslide for two values of the basal residual friction angle.

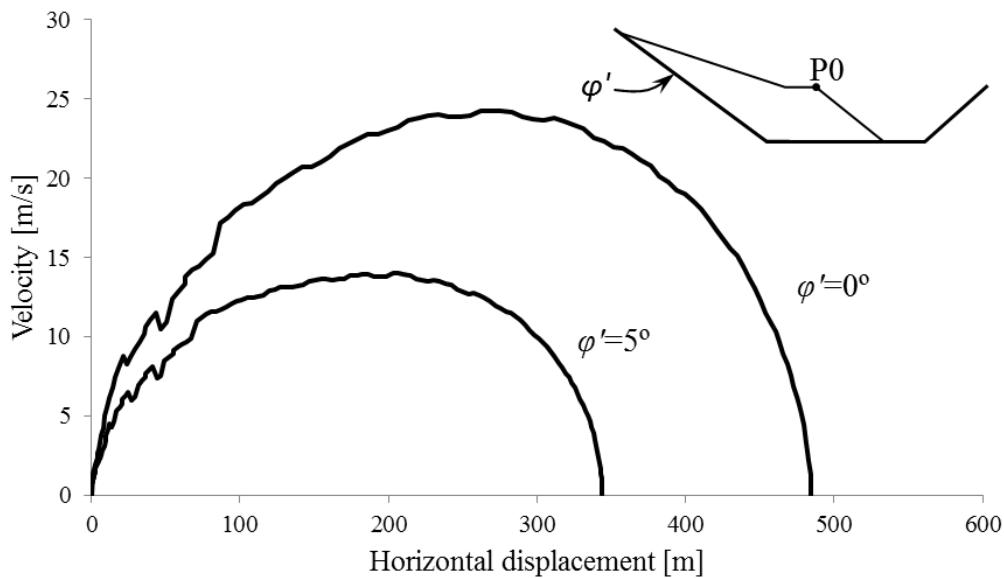


Figure 24. Velocity-displacement response when the basal residual friction is reduced.

Velocity and displacement of point P0 follow the diagram of figure 24. In the case $\phi'_{res_b} = 0^\circ$ the maximum speed is 25m/s, close to the estimations made for Vaiont. The slide reaches the opposite valley slope and has enough inertial energy to climb upwards. Both the maximum velocity and the run-out (490m) are consistent with field observations. The case $\phi'_{res_b} = 5^\circ$ does not explain equally well the actual failure.

The evolution of stresses inside the rock mass may be represented if some points are followed. Figure 25 shows the position of 13 material points located at mid-height at the initial and final states of deformation. The evolution of mobilized friction is shown in figure 26. The first 20s of motion are represented in figure 26a. Peak and residual friction angles provide a reference for the two figures.

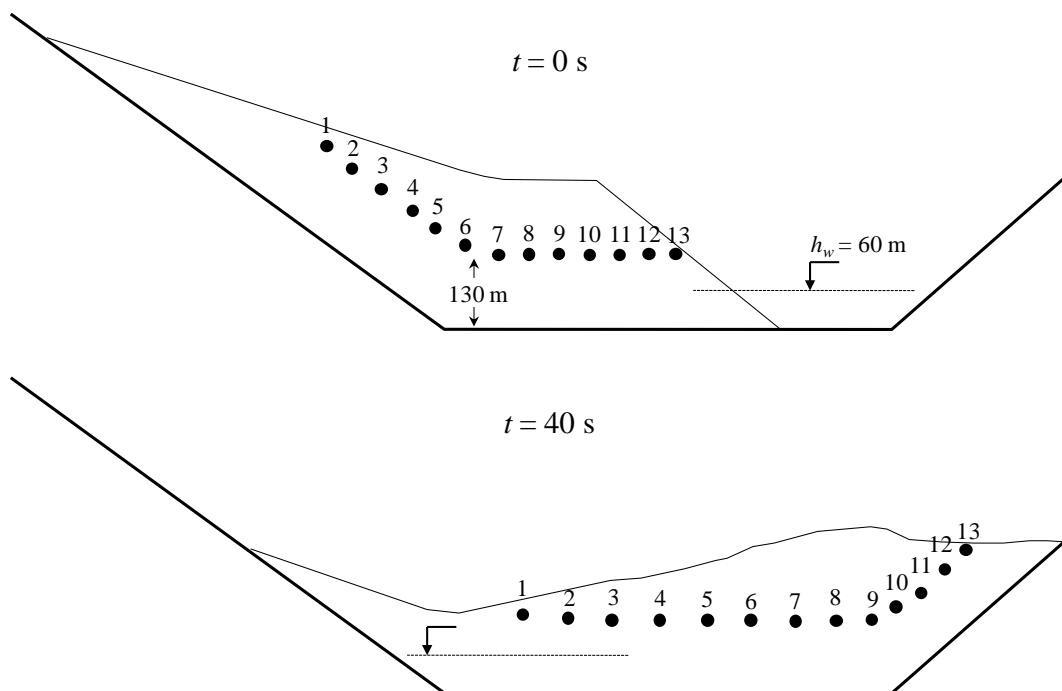


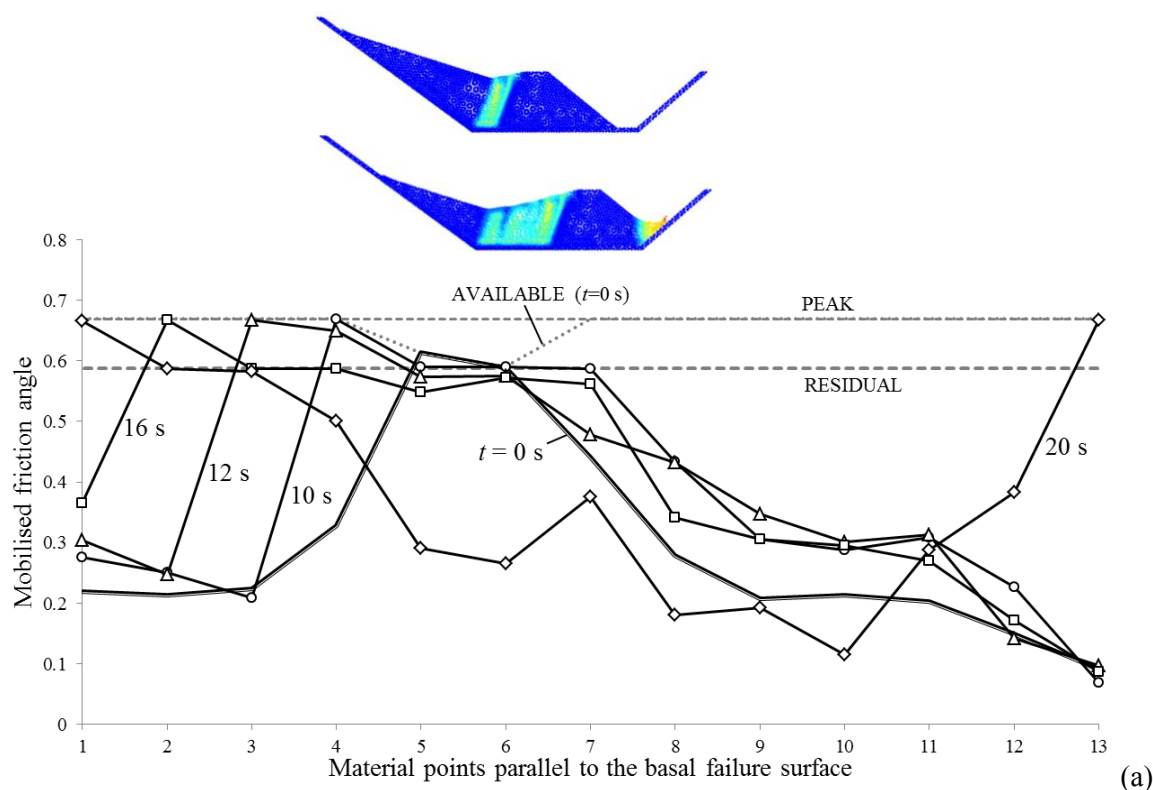
Figure 25. Position of material points selected in the landslide. Zero basal residual friction.

The effect of gravity loading is felt in the vicinity of the internal shearing zone. The available strength for $t = 0$ is lower than the peak strength, as shown in the figure. On both sides of this central zone, the rock remains elastic and the mobilized friction is below the limiting values (peak and residual). The initial stages of the motion damages the rock located on the upward side of the shearing plane. As time increases the process of progressive failure and the transition from elastic to peak and back to residual conditions is illustrated in figure 26. During this period ($t = 0$ to $t = 16$ s), the rock on the right of the shearing plane remains elastic and the mobilized friction remains essentially unchanged because the unstable mass moves forward sliding on a horizontal surface. At $t = 20$ s (figure 26a) point 13 on the toe of the slope “feels” the second change in slope of the basal failure surface and it reaches peak conditions. The remaining stages of the motion are shown in figure 26b. A new process of progressive failure damages the intact rock reaching the position of the second “virtual” shearing plane. At the end of the motion only a small volume of rock roughly located at the position of material points 7 and 8 remains intact. Points 1 to 6, located below the residual mobilized friction, have been unloaded by the new configuration of the slide.

4.3. Final remarks

The example analysed, inspired in a well-known case, illustrates the expected behaviour of brittle rock masses subjected to the kinematics of a compound slide. Internal shearing is probably required for the stability in case of reactivation of the landslides, especially if the basal surface exhibits a low frictional resistance (high plasticity clays).

Progressive failure phenomena are controlled by the kinematics of the motion, which, in turn, are dependent on the geometry of the sliding surface. Exhaustion of available peak strength and the sudden transition to residual conditions explain the initial acceleration of the landslide.



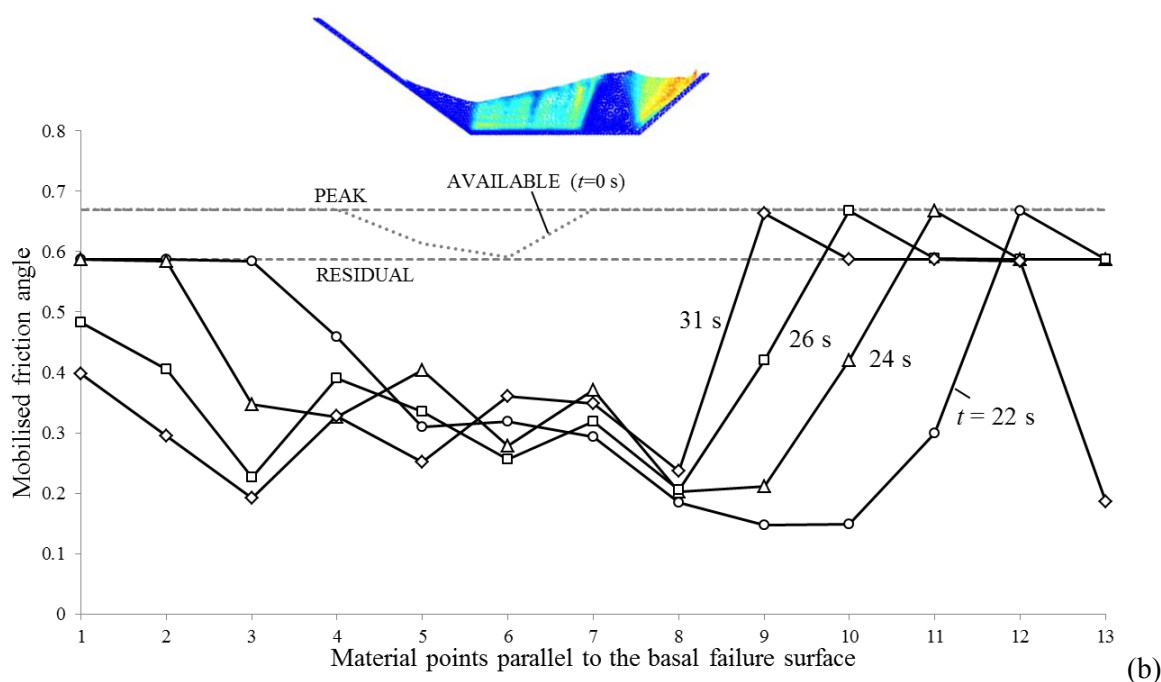


Figure 26. Evolution of mobilized friction angle on selected points. (a) Early stages of deformation; (b) final stages of deformation

In the simple geometrical configuration analysed, the development of an admissible mechanism is internally solved by a single shearing plane, which originates at the sharp transition between the two planes of different inclination. This was a simplified “a priori” choice in the thermomechanical analysis described by Alonso & Pinyol [19], which now receives some support. However, relatively minor changes in the geometry of the sliding surface will most probably lead to different admissible mechanisms. It has also been shown that the very high velocity reached by slides such as Vaiont can hardly be explained only by internal mechanisms of progressive failure. The analysis presented is also a support to phenomena leading to a zero friction basal surface, such as the thermal pressurization of the pore water in the main sliding surface.

5. Rainfall induced landslides

The general formulation for unsaturated soils described in section 2 is applied to simple slope geometry (figure 27). The case is directly based, especially as far as soil properties is concerned, on the analysis of a case history (“Collapse of compacted soil: Girona road embankments, Spain”) presented by [26].

The set of material properties is given in table 3. The computational mesh is made of 3,654 tetrahedral elements. 7,593 material points define the soil mass. A small damping factor ($\alpha = 5\%$) was used in calculations. The time step was $\Delta t = 2 \times 10^{-4}$ s.

The water retention curve (a one-to-one relationship between suction and degree of saturation) for wetting conditions is shown in figure 28. The points in the plot are actual laboratory determinations of the embankment soils: residual soils from granite. They are described as sandy clays of low to medium plasticity.

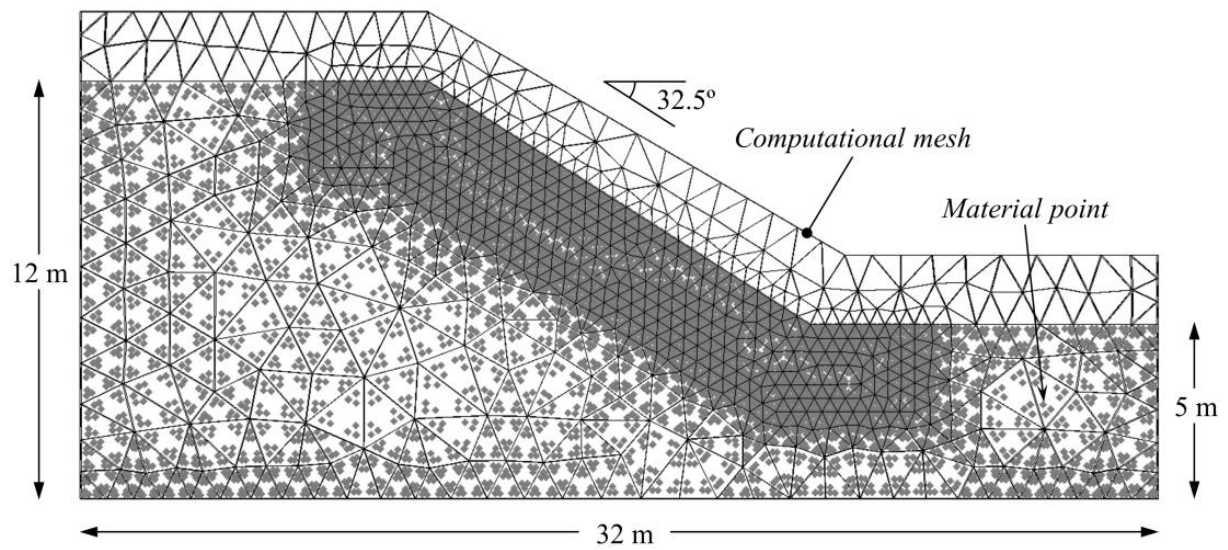


Figure 27. Slope geometry for the rain infiltration case.

Table 3. Mesh details and material properties.

Element type	Tetrahedron
Number of elements	3,654
Number of material points	7,593
Damping factor, α	0.05
Time step	2×10^{-4} s
Solid density, ρ_s	$2,700 \text{ kg/m}^3$
Porosity, n	0.35
Poisson ratio, ν	0.33
Liquid density, ρ_l	$1,000 \text{ kg/m}^3$
Liquid density, ρ_g	1 kg/m^3
Liquid bulk modulus, K_l	100MPa
Gas bulk modulus, K_g	0.01MPa
Liquid viscosity, μ_l	$10^{-3} \text{ kg/m}\cdot\text{s}$
Gas viscosity, μ_g	$10^{-6} \text{ kg/m}\cdot\text{s}$
Intrinsic permeability liquid, k_l	10^{-10} m^2
Intrinsic permeability gas, k_g	10^{-11} m^2
Young modulus, E	10MPa
Effective cohesion, c'	1kPa
Effective friction angle, ϕ'	20°
Δc_{max}	15kPa
B	0.0007
A	0.0001

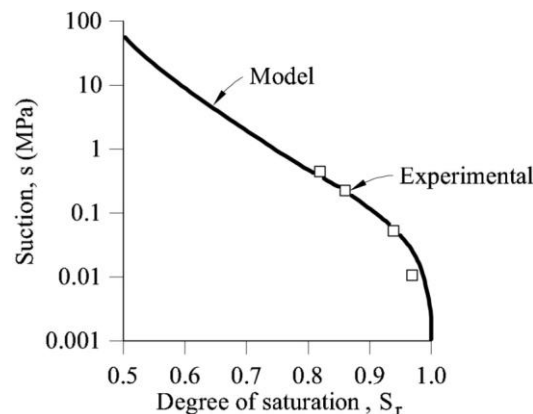


Figure 28. Water retention curve.

The embankment was compacted in summer time and measured water contents in samples recovered indicated that the initial suction was in the range of 700–800 kPa. The initial state of the simulation performed was achieved by imposing equilibrium conditions under boundary suction of 800kPa and a gravity force.

The slopes experienced in the field frequent shallow slides (as well as internal collapse, not analysed here) when they received a series of heavy rains in a relatively short intervals (1–3 days).

The model slope was subjected to a boundary saturation (suction = 0) which was shorter than the actual field conditions. Model permeability was increased to reduce calculation times.

The effect of suction reduction (see section 2) on strength is controlled by the A , B and Δc_{max} parameters in table 3. In other words, a reduction in suction from 800kPa to saturated conditions reduces the cohesion from 67kPa to 1kPa. Friction reduces slightly (less than 1°).

5.1. Model results

The effect of boundary wetting is shown in figure 29. As suction reduces throughout the slope, a shallow shear band develops. The four points selected to show the soil displacements (S_1 , D_1 at the toe of the slope and S_2 , D_2 at mid height) illustrate the slope behaviour. Maximum displacements parallel to the slope surface develop at mid height in shallow locations. Points at the slope foot remain essentially still: they are covered by soil made unstable at higher elevations. At the end of the deformation, the slope angle decreases a few degrees.

Shallow positions (S_2 , S_1) experience a faster reduction in suction and a faster increase in saturation than deeper points. This is shown in figure 30. The first stages of wetting induce fast changes in suction and saturation because of the high pressure gradients involved. The rate of change of suction and saturation decreases continuously, in a non-linear way, during the wetting process.

Information on the dynamics of the motion is one of the key features of MPM. Wetting the slope changes the stress-pore water pressure conditions during a certain time in which sliding displacements are very small. The instability develops suddenly when suction has reduced to low values at shallow depths. This is illustrated in figure 31, which could be compared with figure 30 (a series of common time instants have been indicated in both figures). Dynamic variables depend markedly on the position of the selected control points within the slope. The point at mid slope in a shallow position displaces more and reaches higher maximum velocities and accelerations than other points in the slope. The final part of the motion is characterized by a slow reduction in velocity (slow deceleration). Note that the concept of run-out requires some previous conventions to be defined unambiguously. In general terms, all the points involved in the motion travel different distances. One possible definition of run-out is the distance between the toes of the initial and final slope geometry. In the example solved this distance is 2.5m. However, the maximum (horizontal) displacement of surface points at mid-height is more than 4m.

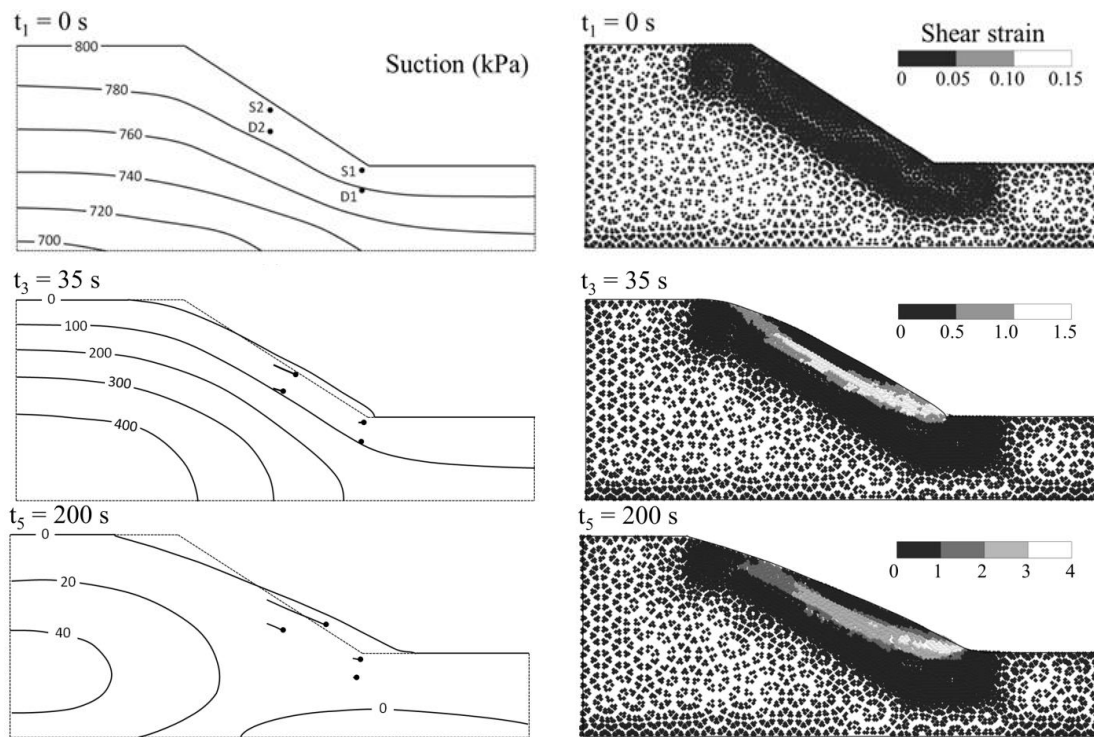


Figure 29. Evolution of suction distribution and deformation of the slope.

The stress paths experienced by the four reference points are also of interest. They are given in a (net mean stress: \bar{p} ; deviatoric stress: q) plane in figure 32. Also plotted in these two figures are the strength envelopes for different suctions.

Point S1, at the toe of the slope is highly stressed and it is initially ($t = t_1$) at yielding conditions. When wetting starts, the stress state in this point changes fast. Local yielding explains the drop in net mean stress (total stress in this case). In addition q decreases following the evolution of strength envelopes. When point S1 is “buried” by the unstable slope at times $t > t_2$, the mean total stress increases and the point remains at yielding conditions for a saturated state.

Point S2 is initially in an elastic state far from yielding conditions for $s = 800\text{kPa}$. Suction reduction brings the yielding envelope to the proximity of the stress state of S_2 , which does not change much during the slope motion because point S2 is above the sliding surface.

Point D1 is in a stable location, below the sliding surface and away from the singularity provided by the toe of the slope. Therefore it is initially under elastic conditions, far from the current yield locus at $t = t_1$. Wetting brings down the yield surface and induces a small increase in (q, p) . The subsequent sliding adds soil weight over point D1, which remains in an elastic state. Finally, point D2 is initially under elastic conditions but when suction decreases it reaches yielding conditions, which remain during the subsequent sliding (D2 is at the shear band).

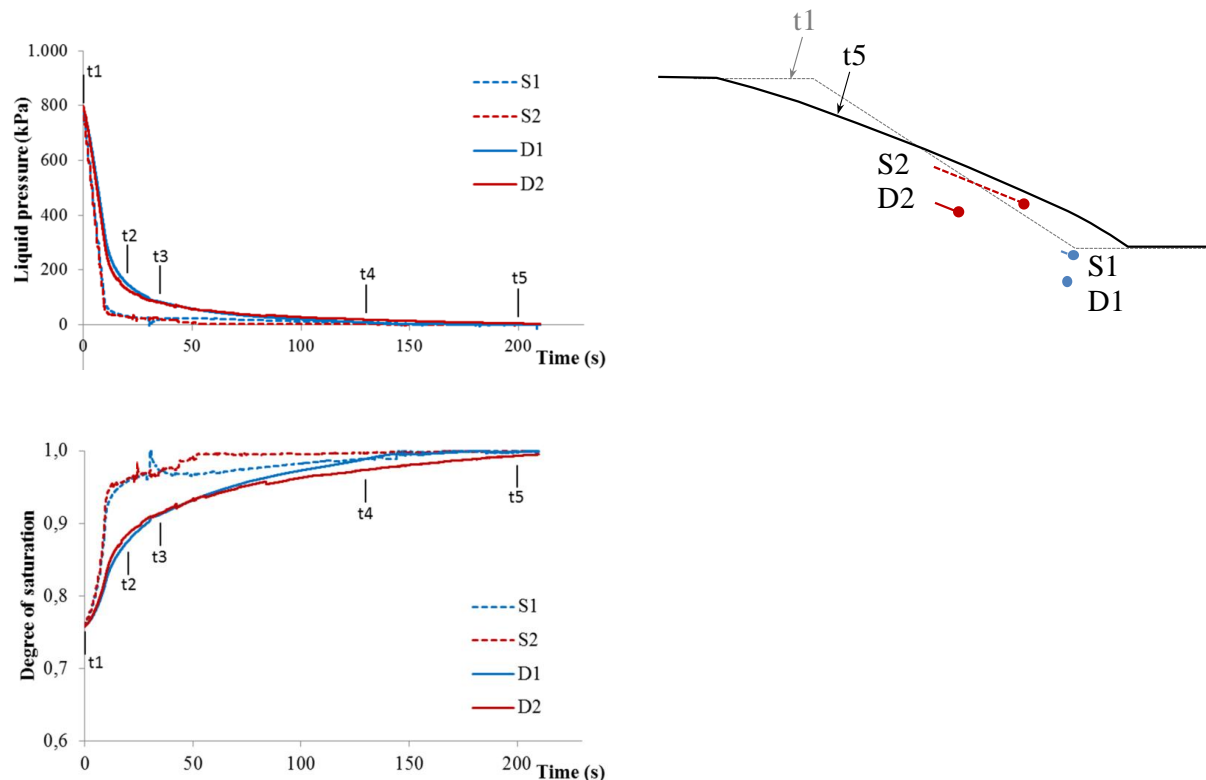


Figure 30. Evolution of suction and degree of saturation for some selected points.

MPM suffers from oscillations of field variables because of the dynamic nature of the formulation. Unbalanced forces, either internal or external, generate waves that cross the domain and may reflect at boundaries. Decrease of stress levels due to softening may be one cause for oscillations. Calculated results show these oscillations. This is shown in figure 33a, which shows the evolution of the deviatoric stress of points D1 and D2. Point D1 shows these oscillations at the later stages of wetting. However, the main reason for this behaviour may be another one. Figure 33b shows evolution of degree of saturation of the two points. Point D1 reaches saturation beyond time t_4 . In fact, the initiation of the oscillatory behaviour seems to coincide with the condition $S_r = 1$ (saturated conditions).

It turns out that the bulk modulus of compressibility of an unsaturated soil increases fast when saturation approaches. This is illustrated in figure 34. The curve in the figure is described by the equation (21) [27].

$$K_m = K_s + \frac{1}{\frac{n S_l}{K_l} + \frac{n(1-S_l)}{K_g}} \quad (21)$$

$$K_{sat} = K_s + \frac{K_l}{n} \quad (22)$$

where K_l , K_s and K_g are the bulk modulus of liquid, solid and gas and S_l the degree of saturation.

The stiffness of the mixture increases abruptly towards the stiffness for saturated conditions (equation (22)), for degrees of saturation in excess of $S_l = 0.99$. This is explained because the bulk modulus of gas is several orders of magnitude smaller than the modulus of liquid water and soil skeleton. Figure 33 shows that the instabilities manifest when the degree of saturation approaches 1.

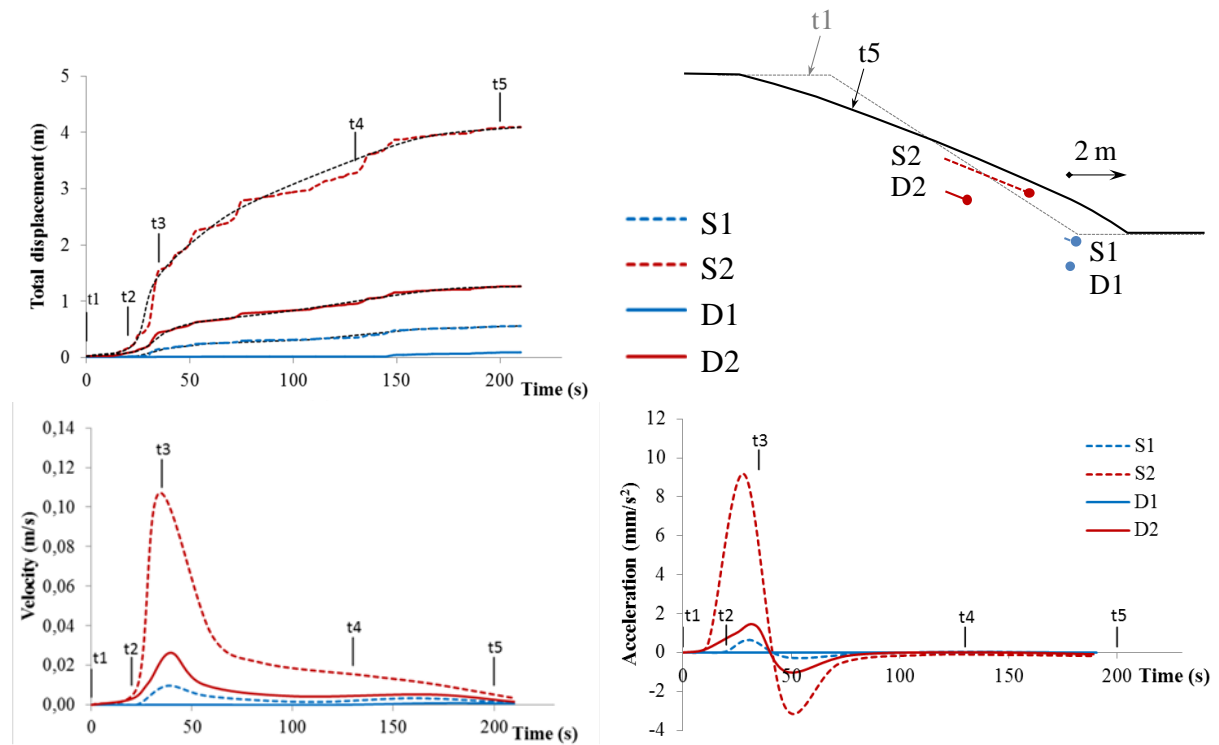


Figure 5.5. Dynamics of the motion.

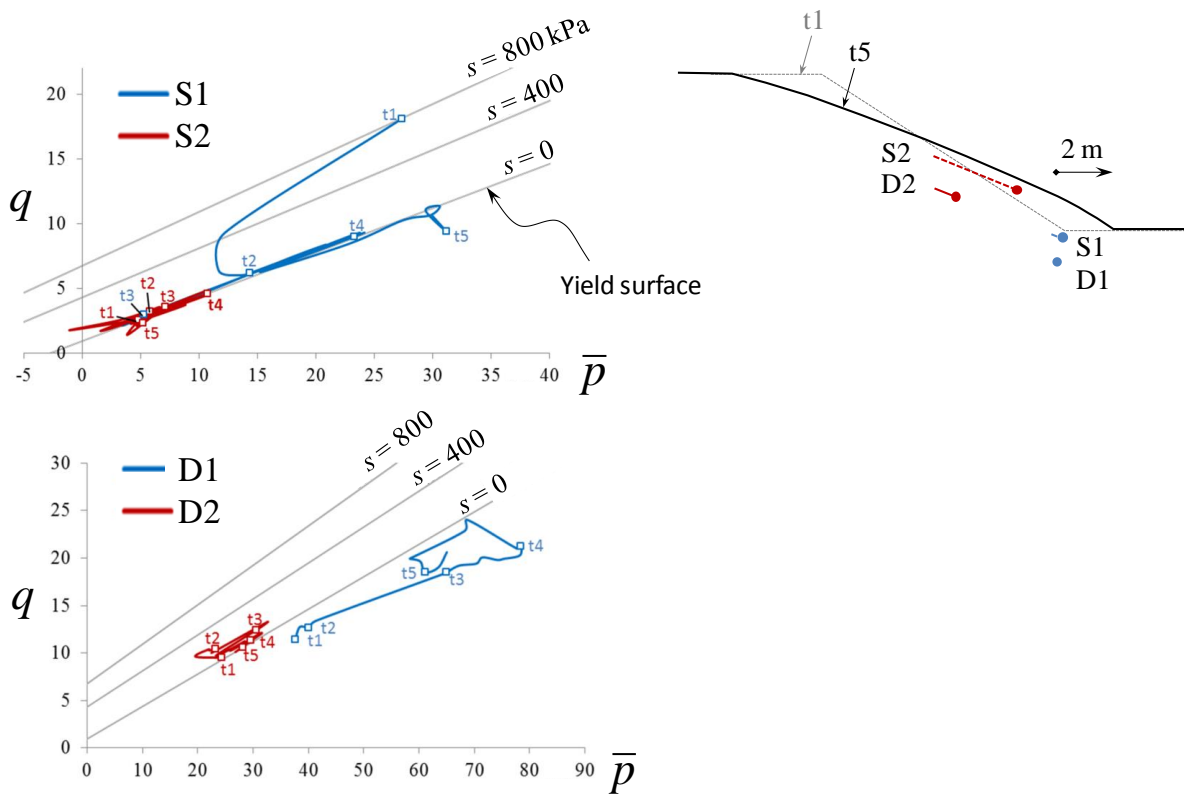


Figure 32. Stress-suction paths of four points within the slope.

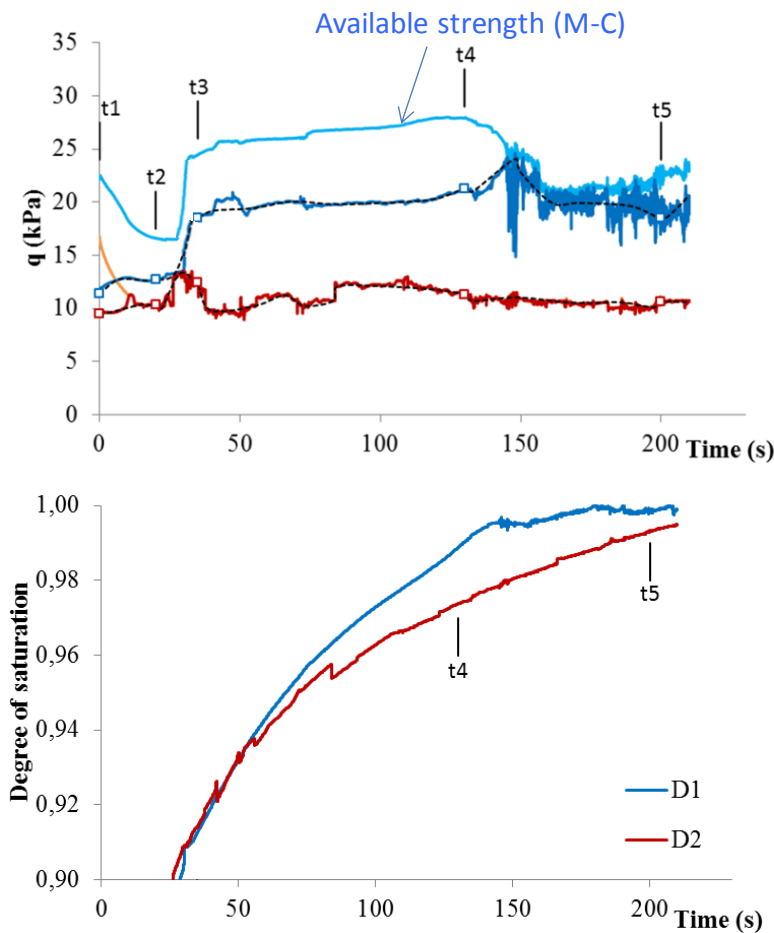


Figure 33. Evolution of deviatoric stress and degree of saturation of points D1 and D2.

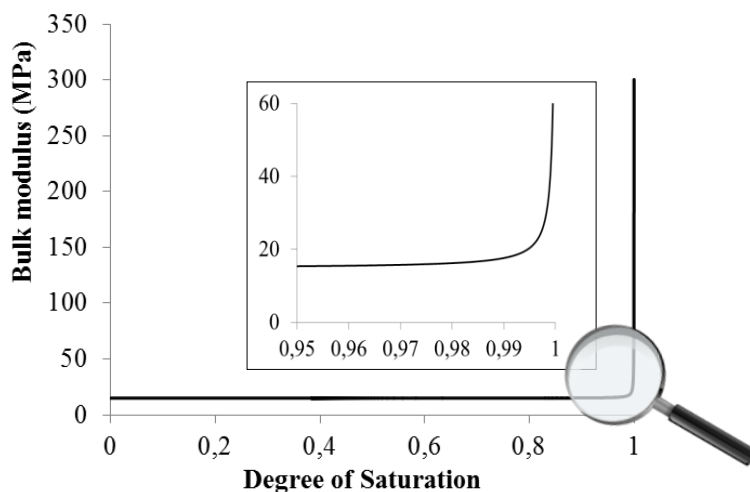


Figure 34. Bulk modulus of unsaturated soil in terms of degree of saturation.

6. Concluding remarks

The MPM and its different formulations for multiphase materials are currently being developed and applied to a variety of geotechnical situations. The MPM concept offers some advantages: being a method for the analysis of continua, it allows the incorporation of the experience gained in finite element analysis; soil behaviour is introduced through well-known constitutive equations (unlike pure particle methods); its dynamic formulation introduces inertia forces and therefore it is well adapted to

analyse post-failure motions and, in the case of landslides, to predict run-out and velocity, two variables directly associated with risk.

A comprehensive MPM formulation for three phase materials coexisting in single material points was presented. Dry and saturated soils are particular cases. The soil models introduced are essentially elastoplastic Mohr-Coulomb formulations. Relevant features are strain softening behaviour and suction dependant strength parameters.

The resulting model provides a unified procedure to examine the static conditions for equilibrium, the transition to an accelerated motion and the propagation of the landslide.

Three cases have been analysed, all of them based on real cases:

The Selborne failure experiment in overconsolidated brittle high plasticity clays provided a further insight into a well-known case of progressive failure development. The MPM model, based on published material properties, slope geometry and hydraulic overpressure inducing failure provided remarkably consistent results. Run-out was successfully reproduced.

The second case examines the role of internal shearing in compound landslides. Vaiont landslide was analysed from this perspective. This is also a case of progressive failure and a final accelerated motion. The damage of the rock could be followed during the sliding motion. It was also found that the very high estimated velocity of the slide could only be reproduced by a zero friction at the basal surface, a result that supports the thermal pressurization hypothesis to explain the full drop of shear strength at the sliding surface.

The third case analyses rainfall effects on a slope whose properties correspond to an embankment slope heavily damaged by intense rainfall. Stress paths of significant points within the slope indicate the complex interaction between stress and suction changes. The dynamic post-failure analysis illustrated the evolution of the slope geometry. Some numerical difficulties are thought to be a consequence of the very fast increase in bulk modulus of the soil when degree of saturation approaches unity.

References

- [1] Sulsky D, Chen Z and Schreyer H L 1994 A particle method for history-dependent materials. *Comp. Met. App. Mec. Eng.* **118** 179–96
- [2] Sulsky D, Zhou S-J and Schreyer H L 1995 Application of a particle-in-cell method to solid mechanics. *Comp. Phys. Comm.* **87** 236–52
- [3] Zhang H W, Wang K P and Chen Z 2009 Material point method for dynamic analysis of saturated porous media under external contact/impact of solid bodies. *Comp. Met. App. Mec. Eng.* **198** 1456–72
- [4] Zabala F and Alonso E E 2011 Progressive failure of Aznalcóllar dam using the material point method. *Géotech.* **61** 795–808
- [5] Jassim I, Stolle D and Vermeer P 2013 Two-phase dynamic analysis by material point method. *Int. J. Num. Anal. Meth. Geomec.* **37** 2502–22
- [6] Yerro A, Alonso E and Pinyol N 2015 The material point method for unsaturated soils. *Géotech.* **65** 201–17
- [7] Abe K, Soga K and Bandara S 2013 Material point method for coupled hydromechanical problems. *J. Geotech. Geoenv. Eng.* **140** 1–16
- [8] Bandara S and Soga K 2015 Coupling of soil deformation and pore fluid flow using material point method. *Comp. Geotech.* **63** 199–214
- [9] Fredlund D G, Morgenstern N R and Widger R A 1978 The shear strength of unsaturated soils. *Can. Geotech. J.* **15** 313–21
- [10] Delage P and Graham J 1996 Mechanical behaviour of unsaturated soils. *Proc. 1st Int. Conf. Unsaturated Soils* (Paris, France, 6–8 Sep 1995) ed E E Alonso and P Delage (Rotterdam, Balkema) pp. 1223–56
- [11] Yerro A, Alonso E and Pinyol N 2014 Modelling progressive failure with MPM. *Proc. 8th Eur. Conf. Numerical Methods in Geotechnical Engineering* (Delft, The Netherlands, 18–20 June

- 2014) ed M A Hicks et al (London, CRC Press) pp 319–23
- [12] Alonso E and Gens A (19??)
- [13] Cooper M, Bromhead E, Petley D and Grant D 1998 The Selborne cutting stability experiment. *Géotech.* **48** 83–101
- [14] Grant D 1996 *Instrumentation systems for and failure mechanisms of an induced slope failure project*. University of Southampton
- [15] Cooper M 1996 The progressive development of a failure slip surface in over-consolidated clay at Selborne, UK. *Proc. 7th Int. Symp. Landslides* (Trondheim, Norway, 17–21 June 1996) ed K Senneset (Rotterdam: Balkema) vol 2 pp 683–688
- [16] Hungr O, Leroueil S and Picarelli L 2014 The Varnes classification of landslide types, an update. *Landslides* **11** 167–194
- [17] Pinyol N M and Alonso E E 2010a Fast planar slides. A closed-form thermo-hydro-mechanical solution. *Int. J. Num. Anal. Meth. Geomech.* **34** 27–52
- [18] Hendron A J and Patton F D 1987 The Vaiont slide. A geotechnical analysis based on new geologic observations of the failure surface. *Engineering Geology* **24** 475–491
- [19] Voigt B and Faust C 1982 Frictional heat and strength loss in some rapid landslides. *Géotech.* **32** 43–54
- [20] Vardoulakis I 2002 Dynamic thermo-poro-mechanical analysis of catastrophic landslides. *Géotech.* **52** 157–171
- [21] Veveakis E, Vardoulakis I and Di Toro G 2007 Thermoporomechanics of creeping landslides: The 1963 Vaiont slide, northern Italy. *J. Geoph. Res* **112** F03026
- [22] Pinyol N M and Alonso E E 2010 Criteria for rapid sliding II. *Eng. Geol.* **114** 211–227
- [23] Pinyol N M and Alonso E E 2010 Fast planar slides. A closed-form thermo-hydro-mechanical solution. *Int. J. Num. Anal. Meth. Geomech.* **34** 27–52
- [24] Cecinato F and Zervos A 2012 Influence of thermomechanics in the catastrophic collapse of planar landslides. *Can. Geotech. J.* **49** 207–225
- [25] Alonso E E and Pinyol N M 2010 Criteria for rapid sliding I. A review of Vaiont case. *Eng. Geol.* **114** 198–210
- [26] Alonso E E, Pinyol N M and Puzrin A M 2010 *Geomechanics of Failures. Advanced Topics* (The Netherlands, Springer)
- [27] Santamarina J C 2001 *Soils and waves* (Berlin, Wiley)